Angular momentum based-analysis of gas-solid fluidized beds in vortex chambers

Angular Momentum Based-Analysis of Gas-Solid Fluidized Beds in Vortex Chambers

Alberto Orozco first draft	August 27
AGQ revision	September 8
Alberto Orozco adjustments	September 9
PP	September 2, 2022

Angular Momentum Based-Analysis of Gas-Solid Fluidized Beds in Vortex Chambers

KEYWORDS: vortex flow; fluidization; Process Intensification; centrifugal force; swirling flow; rotating fluidized bed

Journal: Chemical Engineering Journal, Impact Factor 17.744, cite score 19.4, Q1 top 4 in Chemical Engineering

Journal: Powder Technology, Impact Factor 5.64, cite score 8.4, Q1 top 4 in Chemical Engineering

Highlights

Graphical abstract

1 ABSTRACT

Gas-solid vortex chambers are a promising alternative for reactive and non-reactive processes requiring enhanced heat and mass transfer rates and order-of-milliseconds contact time. The conservation of angular momentum is instrumental in understanding how the interactions between gas, particulate solids, and chamber walls influence the formation of a rotating solids bed. Therefore, this work applies the conservation of angular momentum to derive a model that gives the average angular velocity of solids in terms of gas injection velocity, wall-solids bed drag coefficient, gas and particle properties, and chamber geometry. Three datasets from published studies, comprising 1g-Geldart B- and D-type particles in different vortex chambers, validate the model results. Using a sensitivity analysis, we assessed the effect of input variables on the average angular velocity of solids, average void fraction, and average bed height. Results indicate that the top and bottom end-wall boundaries exert the most significant braking effect on the rotating solids bed compared with the cylindrical outer wall and gas injection boundaries. The wall-solids bed drag coefficient appears independent of the gas injection velocity for a wide range of operating conditions. The proposed model is a valuable tool for analyzing and comparing gas-solid vortex typologies, unraveling improvement opportunities, and scale-up.

2 NOMENCLATURE

Latin characters:

A	Surface area of the boundary wall	m^2
$\bar{a}_c$	Average centripetal acceleration at the bed's center of mass	$m\ s^{-2}$
C_f	Wall-bed drag coefficient	$-$
D	Chamber diameter	m
d_p	Average particle diameter	m
F	External force	N
G	Centrifugal field intensity	$-$
h	Average bed height	m
$\dot{H}$	Rate of change of angular momentum	$kg\ m^2\ s^{-2}$
I_0	Injection slit width	m
I_N	Number of injection slits	$-$
K_{wall}	Wall superficial parameter	$-$
k	Gas injection expansion factor	$-$
k_s	Wall roughness	m
L_R	Chamber length	m
$\dot{m}_g$	Gas mass flow rate	$kg\ s^{-1}$
$\mathcal{M}$	Moment of a force about the chamber's axis	$N\ m$
M_s	Chamber solids loading	kg
M_s^{max}	Maximum solids loading	kg
m_s	Solid mass in the control volume	kg
P	Gas gauge pressure	Pa
r	Radial coordinate	m
r_b	Average radius of the bed inner edge	m
R	Chamber radius	m
Re_θ	Azimuthal Reynolds number for the gas at the injection	$Re_\theta = \frac{\rho_g v_{in} \cos\gamma\, R}{\mu_g}$
Re_p	Particle Reynolds number	$Re_p = \frac{\rho_s d_p v_{r,sup}}{\mu_g}$
S	Swirl ratio	$S = \frac{2\pi R \cos\gamma}{I_N I_0}$
St_{GSVR}	GSVR Stokes number	$St_{GSVR} = \frac{\rho_s d_p^2 v_{in}}{18\mu_g (R - r_b) S}$
u	Particle velocity	$m\ s^{-1}$
$\bar{u}_{\theta_{\bar{r}}}$	Radially averaged solids azimuthal velocity	$m\ s^{-1}$
v	Gas velocity	$m\ s^{-1}$
V_b	Volume of the control volume	m^3

Greek characters:

α	Control volume's sector angle	Rad
β	Interphase momentum transfer coefficient	$kg\ m^{-3}\ s^{-1}$
γ	Injection slit angle with respect to the tangent	Rad
Γ	Angular momentum circulation	$m^2\ s^{-1}$
ε_g	Volumetrically averaged void fraction	$-$
θ	Injection slit projection angle	Rad
μ_g	Gas viscosity	$kg\ m^{-1}\ s^{-1}$
ρ	Density	$kg\ m^{-3}$
$\bar{\rho}$	Biphasic flow density	$kg\ m^{-3}$
τ_w	Wall shear stress	$N\ m^{-2}$
φ	Outlet angle of the gas phase	Rad
χ	Gas-phase attenuation	$-$
$\bar{\omega}$	Solids bed average angular velocity	$Rad\ s^{-1}$

- *Subscript:*

ch	Chimney
cm	Center of mass
$drag$	Gas-solid drag
E	Ergun
ew	End wall
G	Gibilaro
g	Gaseous
go	Gas-only
$grav$	Gravitational
i	Incoming
in	Gas injection
o	Outgoing
ow	Outer wall
r	Radial direction
s	Solids
$static$	Static
sup	Superficial
θ	Azimuthal direction

- *Abbreviations:*

CFB	Conventional Fluidized Beds
CFD	Computer Fluid Dynamics
CV	Control Volume
DEM	Discrete Element Method
GSVR	Gas-Solid Vortex Reactor

GVU	Gas Vortex Unit
HDPE	High Density Polyethylene
PC	Polycarbonate
PI	Process Intensification
RFB	Rotating Fluidized Bed
VC	Vortex Chamber
VFB	Vibrating Fluidized Bed

3 INTRODUCTION

Gas-solid vortex chambers are static centrifugal contactors that generate a rotating solids bed via tangential gas injection from its cylindrical outer wall. These devices can potentially extend and surpass the operational range of conventional fluidized beds by enabling centrifugal accelerations much higher than Earth gravity, which enhances heat and mass transfer rates [1]. Previous analytical approaches to the hydrodynamics of gas-solid vortex chambers include the maximum retention capacity by Sazhin et al. [2], the drag model, and the maximum solids capacity by Friedle et al. [3], [4], and the average angular velocity model using the gas-solid tangential slip factor by de Wilde and de Broqueville [5]. However, according to Kuzmin [6], there is still a lack of predictive methods to calculate swirl flow characteristics, especially multiphase ones. This knowledge gap hinders the development and deployment of such flows despite their significant Process Intensification (PI) potential.

Influential efforts toward an analytical treatment of multiphasic swirling flow in vortex chambers can be traced down to Rosenzweig et al. [7] and Wormley [8] in the ’60s. Those studies used integral angular momentum balances to estimate the pressure and velocity profiles, starting from Navier-Stokes’ equations. However, those analytical approaches suffer from oversimplifications and mathematical complexity, making them intractable and impractical by today’s Computational Fluid Dynamics (CFD) standards. That is not to say these efforts have been in vain. For example, Volchkov [9] and Goldshtik [10] have made outstanding advancements in the theoretical understanding of vortex chamber phenomena using this very same approach.

The angular momentum balance developed by Anderson et al. [11] in the ’70s fits the experimental results from the colloid core vortex nuclear reactor. The model predicts crucial hydrodynamic observables even with limited input data. This convenience contrasts with CFD Euler-Euler approaches, which require calibration against experimental data given the semi-empirical nature of the Johnson-Jackson boundary condition. Furthermore, Euler-Lagrange CFD approaches, such as the CFD-DEM (discrete element method) coupling, are limited to a certain number of particles and require the particle size to be smaller than the grid cell size. This condition is presently unattainable in the gas injection region of vortex chambers because very minute cell sizes are needed to simulate momentum transfer near the slits [12].

The analytical models described above offer ingenious approaches to the complex hydrodynamics of vortex chambers. The gas-solid angular momentum exchange determines

the solids bed hydrodynamics and the response of particles to the incoming gas jets [1]. In this regard, an angular momentum balance may offer robustness, and practical convenience, which is a valuable first step given the complex and computationally expensive CFD procedures, the insurmountable design typologies, and the wide operational ranges.

The proposed model elaborates upon the angular momentum balance for gas-solid vortex chambers developed by Anderson et al. [11] and Smulsky [13]. The model correlates the average solids bed angular velocity $\bar{\omega}$ with gas injection velocity v_{in}, wall-solids bed drag coefficients $C_{f,ow}$, $C_{f,ew}$, solids loading M_s, inner bed edge radius r_b, gas and solids properties, and chamber geometrical parameters. The model encompasses a discrete balance for the outermost bed layer where the outer-wall skin friction $C_{f,ow}$ acts upon, and a continuous balance for top and bottom end walls where the end-wall skin friction $C_{f,ew}$ is dominant.

4 METHODS

4.1 Model assumptions

Vertical axis of rotation

This way, gravitational effects only occur in a plane perpendicular to the bed's rotation with negligible effects on the angular momentum exchange.

Axisymmetrical rotating bed with rigid body-like movement

A specific hydrodynamic regime is assumed, consisting of a compact and uniformly distributed rotating bed with a well-defined inner edge. This regime is attainable for various solid particles with sufficient gas injection velocity and solids loading [14]. Additionally, the azimuthal velocity of particles u_θ follows the rigid body kinematic expression $u_\theta = \bar{\omega} r$. These conditions are widely employed in analytical formulations in vortex chambers and swirling fluidized beds (SFB) [5][15][16][17][18]. This analysis does not consider time-dependent phenomena, particle entrainment, and particle size and density distributions. Consequently, the rotating bed can be considered a series of cells with periodical variations in their hydrodynamic quantities between consecutive slits and continuity at the boundaries between each cell.

Azimuthal no-slip condition between gas and solid phases at the bed edge boundary

A similar boundary condition is found in [11] and [17] for the gas-solid vortex reactor (GSVR) and SFB, respectively. This condition couples the gas azimuthal velocity with the solids bed's rigid body-like rotation at the bed's inner edge boundary in a way that $v_{r_b,\theta} \cong \bar{\omega} r_b$. This assumption comes from the azimuthal gas-solid slip factor s^{gs} introduced by de Wilde et al. [5], which represents a proportionality factor written as $s_{r_b}^{gs} = \frac{\bar{\omega} r_b}{v_{r_b,\theta}}$. Niyogi et al.

[19] reported radial profiles of azimuthal gas-solid slip velocities for 1-g Geldart D-type particles in a wide range of gas injection velocities, for which all the analyzed conditions achieve a zero-slip azimuthal velocity near the inner bed edge. Thus, the azimuthal no-slip condition between phases is applicable for an appropriate bed inner edge radius choice.

Flow symmetry in the axial direction

The gas-solid flow is analyzed for the whole axial length of the bed, considering the friction forces about the end walls, $F_{ew,up}$ and $F_{ew,down}$, as parallel and identical in magnitude. According to Rosales-Trujillo et al. [20], this is a plausible assumption for a sufficiently high gas injection velocity and a dense particle bed. This way, azimuthal velocity gradients in the axial direction and the flow effects of the exhaust are dampened by the rotating solids bed.

Incompressible gas flow

A subsonic flow with $Ma < 0.3$ must be guaranteed; this condition applies to the typical operational range of gas-solid vortex chambers.

4.2 Model derivation

The control volume follows the shape of a symmetric rotating solids bed, resembling a torus of rectangular cross-section, as depicted in **Figure 1**~~**Figure 1**~~. Given appropriate symmetry conditions, the control volume further reduces to an annular sector between two consecutive gas injection slits, as shown in **Figure 2**~~**Figure 2**~~.

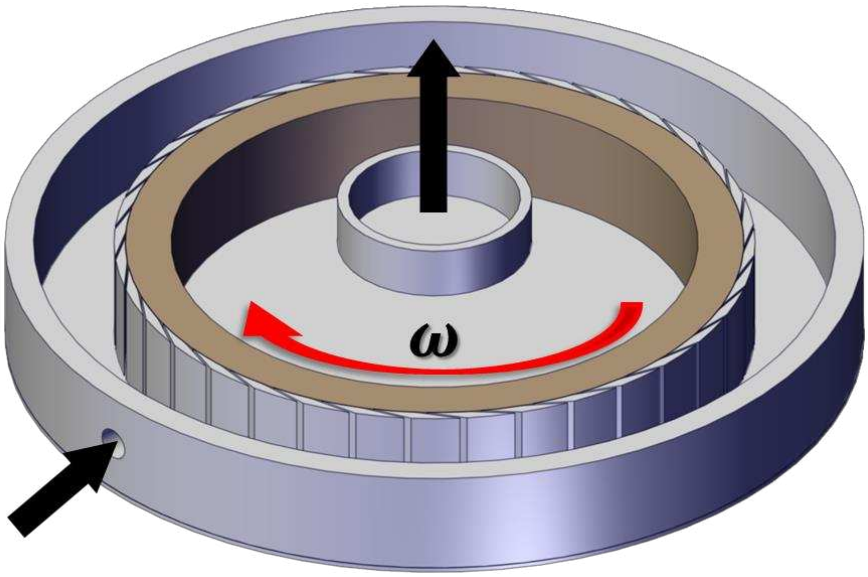

Figure 1 3D representation of the vertical vortex chamber used for the model derivation.

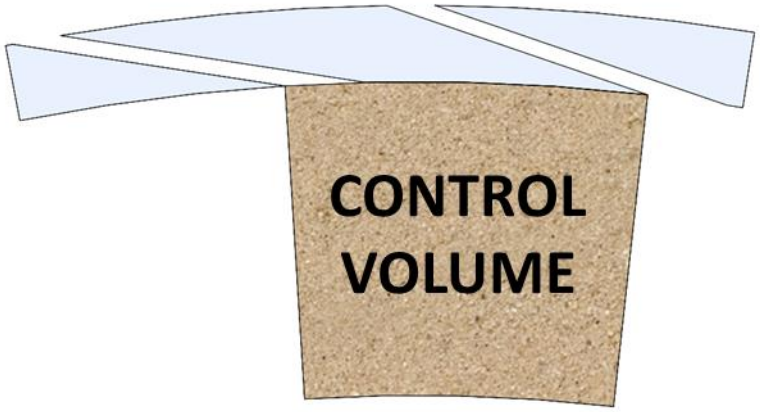

Figure 2 Detailed top-view of CV inter-slit space.

The sector angle α, according to the vortex chamber geometry, is given by Equation 1.

$$\alpha = \frac{2\pi}{I_N} \quad (1)$$

where I_N is the number of gas injection slits.

Equation 2 gives the volume of the vortex chamber V_b.

$$V_b = \frac{1}{2}\alpha(R^2 - r_b^2)L_R \quad (2)$$

where R is the chamber radius, r_b the radius of the inner bed edge, and L_R the chamber length.

Equation 3 gives the solids mass in the control volume m_s.

$$m_s = \frac{M_s}{I_N} \quad (3)$$

where M_s is the solids loading of the vortex chamber.

Equation 4 gives the gas mass flow rate $\dot{m}_g$ for a rectangular slit of dimensions $I_0 \cdot L_R$.

$$\dot{m}_g = \rho_g I_0 L_R v_{in} \quad (4)$$

where ρ_g is the gas density and v_{in} the gas injection velocity.

The volumetrically averaged void fraction of the solids bed ε_g is given by Equation 5.

$$\varepsilon_g = 1 - \frac{V_s}{V_b} = 1 - \frac{m_s}{\rho_s V_b} \quad (5)$$

where V_s and ρ_s are the solids volume and density, respectively.

The average biphasic flow density $\bar{\rho}$ is described by Equation 6.

$$\bar{\rho} = \frac{\rho_s V_s + \rho_g V_g}{V_b} \quad (6)$$

Equation 7 arises from substituting **Equation (6)** in **Equation (5)**.

$$\bar{\rho} = (1 - \varepsilon_g)\rho_s + \varepsilon_g \rho_g \quad (7)$$

Figure 3 depicts a 2D angular momentum diagram. Two forces act upon the boundaries, the friction force on the outer wall F_{ow}, and the friction force on the top and bottom end walls F_{ew}. Figure 3 also illustrates the main mass and angular momentum fluxes through the vortex chamber, expressed in terms of mass flow rates $\dot{m}$ and flow circulation Γ.

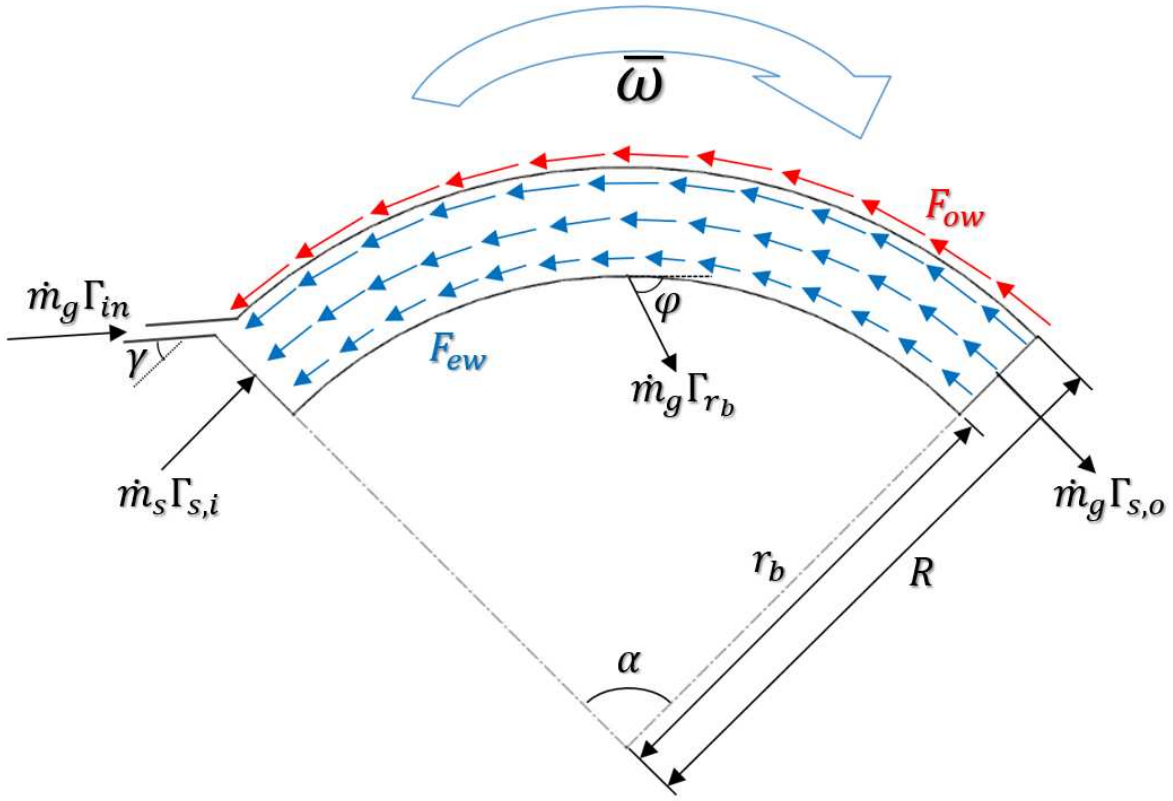

Figure 3 CV's 2D angular momentum diagram. The outer wall curvature has been exaggerated to enhance the visual effect.

The angular momentum balances apply for successive cylindrical surface layers, advancing in the radial direction from the outer wall to the inner bed edge. Discrete and continuous angular momentum balances are necessary to account for F_{ow} and F_{ew}, respectively.

4.2.1 Discrete angular momentum balance for the outer wall

According to Figure 4, the outer wall area A_{ow} given by Equation 8 corresponds to the surface area of the cylindrical outer wall at the chamber radius R.

heeft opma
heeft opma
Cursief, Spel
heeft opma
heeft opma
heeft opma
Cursief, Spel
heeft opma
heeft opma
heeft opma
heeft opma

$$A_{ow} = \alpha' R L_R \quad (8)$$

where α' is the sector angle excluding the injection slit.

Equation 9 gives the sector angle α'.

$$\alpha' = \alpha - \theta \quad (9)$$

where α is the sector angle in **Equation** (1)~~(1)~~ and θ the projected slit angle given by **Equation** (10)~~(10)~~.

$$\theta = cos^{-1}\left[cos\,\gamma - \frac{I_0}{R}\right] - \gamma \quad (10)$$

where γ is the injection slit angle relative to a tangent line.

Equation 11 results from substituting **Equations** (1)~~(1)~~ and (10)~~(10)~~ into **Equation** (9)~~(9)~~.

$$\alpha' = \frac{2\pi}{I_N} - cos^{-1}\left[cos\,\gamma - \frac{I_0}{R}\right] + \gamma \quad (11)$$

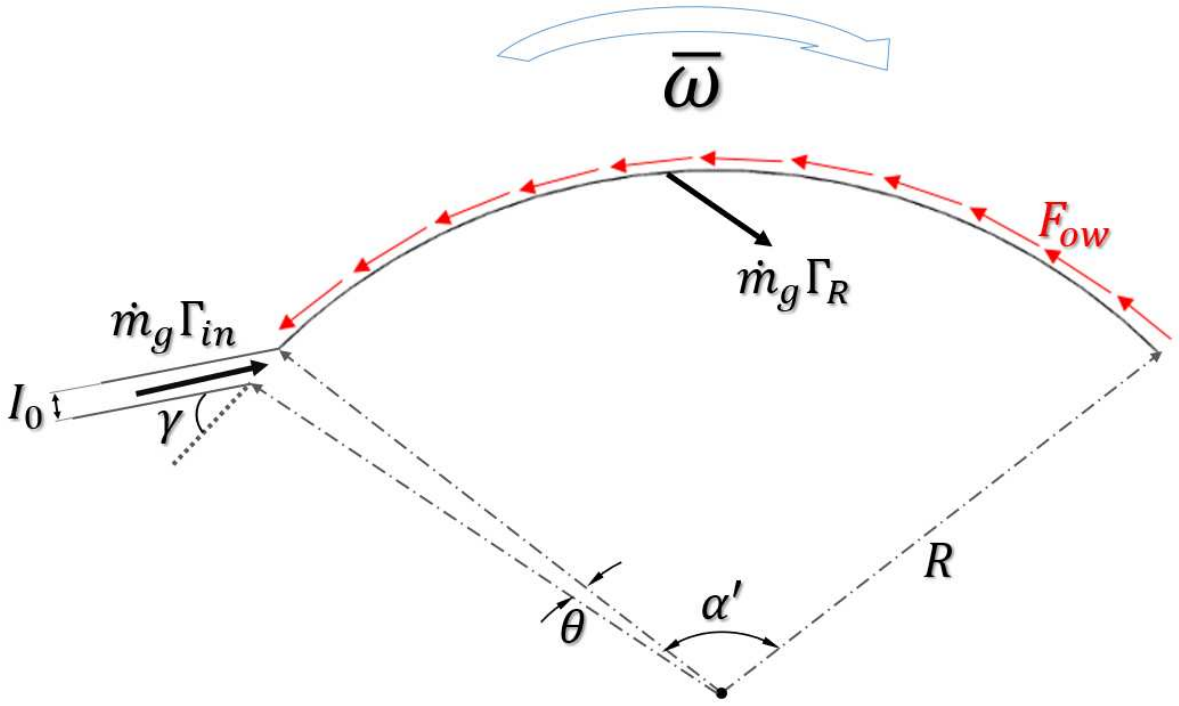

Figure 4 Angular momentum diagram for the outer wall.

Figure 4~~Figure 4~~ also illustrates the angular momentum balance for the outer wall cylindrical indicated by Equation 12.

$$\dot{H}_{in} + \sum \mathcal{M}_{ext} = \dot{H}_R \quad (12)$$

heeft opma
heeft opma Cursief, Spel
heeft opma
heeft opma
heeft opma
heeft opma
heeft opma
heeft opma Cursief, Spel
heeft opma
heeft opma
heeft opma Cursief, Spel
heeft opma
heeft opma
heeft opma Cursief, Spel
heeft opma
heeft opma

where $\sum \mathcal{M}_{ext}$ is the sum of all external torques on the outer wall boundary, $\dot{H}_{in}$ the rate of change of angular momentum of the inlet gas, and $\dot{H}_R$ the rate of change of angular momentum for the gas flowing through the outer layer of the solids bed. Equation 13 with the appropriate subscripts gives $\dot{H}_{in}$ and $\dot{H}_R$.

$$\dot{H} = \dot{m}_g v_\theta r = \dot{m}_g \Gamma \quad (13)$$

where Γ is the angular momentum circulation at radius r, $v_\theta r$. This definition encompasses the azimuthal velocity and lever-arm effects into one variable [11] [13] [21].

Replacing all known variables in **Equation** (12)~~(12)~~ results in Equation 14.

$$\dot{m}_g \Gamma_{in} - \mathcal{M}_{ow} = \dot{m}_g \Gamma_R \quad (14)$$

where Γ_{in} corresponds to $v_{in}\, cos\, \gamma\, R$, and $\mathcal{M}_{ow}$ represents the friction moment about the outer wall.

The friction moment $\mathcal{M}_{ow}$ requires a constitutive equation to model the solids collision and sliding phenomena along with the fluid skin friction and gas jet impingement. Several authors [6] [13] [21] [22] agree that the aerodynamic drag equation is the best suited for modeling, in an approximate fashion, gas-solid and gas-liquid boundary wall interactions in vortex chambers and cyclones. For example, Goldshtik [21] concluded that this Equation overestimates the braking effects on the bed but provides a conservative prediction. Additionally, for an axisymmetrical rotating bed $\mathcal{M}_{ow}$ equals $F_{ow} R$. This way, the outer wall resistive action is independent of the angular position in which it is analyzed, following the axial symmetry assumption. From the drag coefficient definition, the outer wall drag coefficient $C_{f,ow}$ is used to determine F_{ow} as indicated in Equation 16.

$$F_{ow} = C_{f,ow} \frac{\rho_R v_{R,\theta}^2}{2} A_{ow} \quad (15)$$

$C_{f,ow}$ represents the ratio of the outer wall shear stress τ_w to the outer wall normal stress, here described by the flow's dynamic pressure $\frac{1}{2}\rho_R v_{R,\theta}^2$ at the outer wall. **Equation** (15)~~(15)~~ also describes a quadratic dependency of the friction force F_{ow} on the flow's azimuthal velocity at the outer wall layer $v_{R,\theta}$; and a linear dependency on the biphasic flow density at the outer wall layer ρ_R. The latter variable considers the hydrodynamic effects of gas injection on this boundary and relates to the mean biphasic density $\bar{\rho}$ through the gas injection expansion factor k, given by Equation 16.

$$k = \frac{\rho_R}{\bar{\rho}} \quad (16)$$

Here k takes values in the interval $(0,1]$ and describes the increase in void fraction at the outer wall layer once the bed comes into contact with the incoming gas jet. Using X-rays, Anderson et al. [11] observed this expansion in a vortex chamber. However, they did not offer a method for its estimation, assigning a value of 0.1 considering their experimental

heeft opma
heeft opma
heeft opma
heeft opma
heeft opma
heeft opma

findings for 1g-Geldart C-type particles. Niyogi et al. [19] and Vandewalle et al. [12] have also documented this expansion in experimentally validated 3D Euler-Euler CFD simulations, while Gonzalez-Quiroga et al. [1] reported a similar behavior in their observed azimuthal and radial bed voidage patterns. Furthermore, these findings revealed a sinusoidal profile for the azimuthal velocity of solids between consecutive injection slits. Thus, the gas injection expansion factor k could help to quantify the effect of the bed's azimuthal acceleration and deacceleration on the mean angular velocity of the solids bed.

The authors surmise that the expansion factor k should depend on the 1g-Geldart particle type and the mechanisms by which the rotating solids bed interacts with the incoming gas jets. We also conjecture that k's behavior follows a correlation of the type $k = f(Re_\theta, St_{GSVR})$, by analogy with the cyclone's separation efficiency at low solids loadings [22], with the Reynolds and Stokes dimensionless groups arising naturally from the interaction of solid particles and swirling flows. The cyclone's separation efficiency describes the tendency of solid particles to be centrifuged away in the cyclone body, which can simultaneously measure their propensity to follow gas streamlines closely. Dring et al. [23] also analyzed particle trajectories in swirling flows, pointing out that these dimensionless groups describe the interactions between particles and gas streamlines.

According to Smulsky [13], Equation 17 gives the azimuthal Reynolds number for gas injection in a vortex chamber.

$$Re_\theta = \frac{\rho_g (v_{in} \cos\gamma) R}{\mu_g} \quad (17)$$

where μ_g corresponds to the gas viscosity. Equation 18 gives the Stokes number for a GSVR, following Vandewalle et al. [12].

$$St_{GSVR} = \frac{\rho_s d_p^2 v_{in}}{18 \mu_g (R - r_b) S} \quad (18)$$

where d_p is the average particle diameter. Additionally, S represents the swirl ratio, defined as the ratio between the gas azimuthal velocity at the injection $v_{in,\theta}$ and the gas superficial radial velocity at radius R $v_{sup,R}$, as given by Equation 19.

$$S = \frac{v_{in,\theta}}{v_{sup,R}} = \frac{2\pi R \cos\gamma}{I_N I_0} \quad (19)$$

Spherical, dense, and coarse solid particles are more efficient at transferring the gas jet's momentum in fluidized beds [24], a result that has been extended to centrifugal fluidized beds by different authors [12] [25]. Furthermore, de Wilde et al. [5] and Kulkarni et al. [26] found that most of the gas jet's angular momentum transfers to the solids bed in the vicinity of the outer wall, which in turn produces a near radial-like flow pattern for the rest of the gas transit through the solids bed. Nevertheless, further research is needed to unravel the gas jet's

dispersion profile and the degree of local contraction and expansion of the rotating solids bed.

Equation 20 gives the circulation at the radius R, Γ_R.

$$\Gamma_R = v_{R,\theta} R \tag{20}$$

Substituting **Equations** (8)~~(8)~~, (16)~~(16)~~ and (20)~~(20)~~ in **Equation** (15)~~(15)~~ results in Equation 21.

$$\mathcal{M}_{ow} = \frac{1}{2}\alpha' C_{f,ow} k \bar{\rho} L_R \Gamma_R^2 \tag{21}$$

Substituting **Equation** (21)~~(21)~~ in **Equation** (14)~~(14)~~ yields Equation 22.

$$\frac{\alpha' C_{f,ow} k \bar{\rho} L_R}{2\dot{m}_g}\Gamma_R^2 + \Gamma_R - \Gamma_{in} = 0 \tag{22}$$

Solving the quadratic formula for Γ_R and applying the restriction $\Gamma_R \geq 0$ yields Equation 23.

$$\Gamma_R = \frac{\sqrt{1 + \frac{2\alpha' C_{f,ow} k \bar{\rho} L_R \Gamma_{in}}{\dot{m}_g}} - 1}{\frac{\alpha' C_{f,ow} k \bar{\rho} L_R}{\dot{m}_g}} \tag{23}$$

heeft opma
heeft opma Cursief, Spel
heeft opma
heeft opma
heeft opma Cursief, Spel
heeft opma
heeft opma
heeft opma Cursief, Spel
heeft opma
heeft opma
heeft opma
heeft opma
heeft opma
heeft opma
heeft opma
heeft opma Cursief, Spel
heeft opma

4.2.2 Continuous angular momentum balance for the end walls

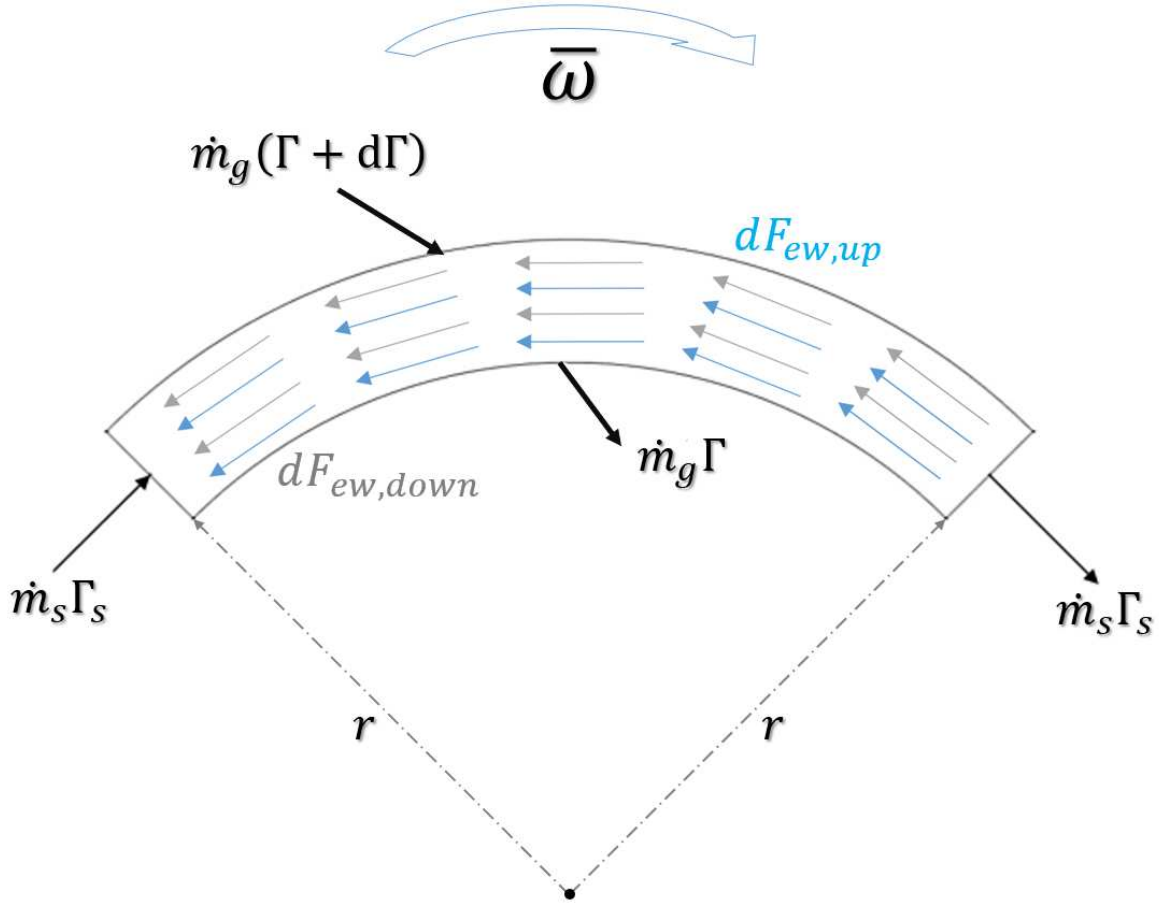

Figure 5 Angular momentum diagram for the end walls.

Figure 5~~**Figure 5**~~ illustrates the angular momentum balance for the bottom and top end walls. For a layer of thickness dr on the interval $r_b \leq r < R$, Equation 24 gives the differential angular momentum balance.

$$d\dot{H}_o - d\dot{H}_i = d\mathcal{M}_{ew} \tag{24}$$

Equation 25 applies for a differential element, considering a compact and axisymmetrical rotating solids bed.

$$\begin{aligned} d\dot{H}_o - d\dot{H}_i &= \left[\dot{m}_g\Gamma + \dot{m}_s\Gamma_s\right] - \left[\dot{m}_g(\Gamma + d\Gamma) + \dot{m}_s\Gamma_s\right] \\ &= -\dot{m}_g\, d\Gamma \end{aligned} \tag{25}$$

Equation 26 gives the resistive friction moment for both end walls.

$$d\mathcal{M}_{ew} = -\left(dF_{ew,up} + dF_{ew,down}\right) * r \tag{26}$$

Both forces are parallel and identical following the flow symmetry in the axial direction assumption, as indicated by Equation 27.

$$d\mathcal{M}_{ew} = -2dF_{ew} * r \tag{27}$$

The aerodynamic drag model for skin friction, given by Equation 28, is employed in its differential form.

$$d\mathcal{M}_{ew} = -2\left(C_{f,ew} * \frac{\bar{\rho} v_\theta^2}{2} * dA_{ew}\right) * r \tag{28}$$

Equation 29 gives the differential end wall area A_{ew}.

$$dA_{ew} = \alpha r dr \tag{29}$$

Replacing **Equation (29)** in **Equation (28)** results in Equation 30.

$$d\mathcal{M}_{ew} = -\alpha \bar{\rho} C_{f,ew} \Gamma^2 dr \tag{30}$$

The end wall drag coefficient $C_{f,ew}$ does not have to be, in principle, identical to its outer wall counterpart $C_{f,ow}$ given the notable differences in hydrodynamic conditions between each boundary. There is no gas injection via the end walls; hence, the mean biphasic flow density $\bar{\rho}$ can be employed without further modifications. Substituting **Equations (25)** and **(30)** in **Equation (24)** yields Equation 31.

$$-\dot{m}_g d\Gamma = -\alpha C_{f,ew} \bar{\rho} \Gamma^2 dr \tag{31}$$

Finally, integrating between the outermost radius R and innermost radius r_b yields Equation 32.

$$\Rightarrow \frac{1}{\Gamma_{r_b}} = \frac{1}{\Gamma_R} + \frac{\alpha C_{f,ew} \bar{\rho} (R - r_b)}{\dot{m}_g} \tag{32}$$

4.2.3 Total angular momentum balance

Equation 33 results from substituting **Equation (23)** in **Equation (32)**.

$$\Gamma_{r_b} = \frac{1}{\dfrac{\dfrac{\alpha' C_{f,ow} k \bar{\rho} L_R}{\dot{m}_g}}{\sqrt{1 + \dfrac{2\alpha' C_{f,ow} k \bar{\rho} L_R \Gamma_{in}}{\dot{m}_g}} - 1} + \dfrac{\alpha C_{f,ew} \bar{\rho} (R - r_b)}{\dot{m}_g}} \tag{33}$$

According to the azimuthal no-slip assumption between phases at the inner edge of the solids bed, the circulation at that position follows Equation 34.

$$\Gamma_{r_b} = v_{r_b,\theta} r_b = \bar{\omega} r_b^2 \tag{34}$$

Therefore **Equation (33)** can be rewritten as Equation 35.

heeft opma
heeft opma
heeft opma
heeft opma
heeft opma
heeft opma
heeft opma
heeft opma
heeft opma
heeft opma
heeft opma
heeft opma
heeft opma
heeft opma
heeft opma Cursief, Spel
heeft opma
heeft opma
heeft opma
heeft opma
heeft opma
heeft opma Cursief, Spel
heeft opma
heeft opma
heeft opma
heeft opma

$$\bar{\omega} r_b^2 = \frac{1}{\frac{\frac{\alpha' C_{f,ow} k \bar{\rho} L_R}{\dot{m}_g}}{\sqrt{1 + \frac{2\alpha' C_{f,ow} k \bar{\rho} L_R \Gamma_{in}}{\dot{m}_g}} - 1} + \frac{\alpha C_{f,ew} \bar{\rho} (R - r_b)}{\dot{m}_g}} \tag{35}$$

Equation 36 results from **Equation (4)~~(4)~~**:

$$\bar{\omega} r_b^2 = \frac{v_{in}}{\frac{\frac{\alpha' C_{f,ow} k \bar{\rho}}{\rho_g I_0}}{\sqrt{1 + 2\frac{\alpha' C_{f,ow} k \bar{\rho}}{\rho_g I_0} \cos\gamma R} - 1} + \frac{\alpha C_{f,ew} \bar{\rho} (R - r_b)}{\rho_g I_0 L_R}} \tag{36}$$

Contrasting **Equation (36)~~(36)~~** with Ohm's law and Fourier's law, a similar analogy can be made for the circulation at the inner edge of the solids bed $\bar{\omega} r_b^2$, the injection velocity v_{in}, and the denominator of the right side of the said Equation 36.

Thus, we introduce three resistances in Equations 37-39, one for each flow boundary.

- Injection resistance $\mathcal{R}_{in}$:

$$\mathcal{R}_{in} = \frac{1}{\cos\gamma R} \tag{37}$$

- Outer wall resistance $\mathcal{R}_{ow}$:

$$\mathcal{R}_{ow} = \frac{\alpha' C_{f,ow} k \bar{\rho}}{\rho_g I_0} \tag{38}$$

- Outer wall resistance $\mathcal{R}_{ew}$:

$$\mathcal{R}_{ew} = \frac{\alpha C_{f,ew} \bar{\rho} (R - r_b)}{\rho_g I_0 L_R} \tag{39}$$

Finally, substituting **Equations (37)~~(37)~~**, **(38)~~(38)~~,** and **(39)~~(39)~~** in **Equation (36)~~(36)~~** yields Equation 40.

$$\bar{\omega} r_b^2 = \frac{v_{in}}{\left(\frac{\mathcal{R}_{ow}}{\sqrt{1 + 2\frac{\mathcal{R}_{ow}}{\mathcal{R}_{in}}} - 1} + \mathcal{R}_{ew} \right)} \tag{40}$$

Equation (40)~~(40)~~ synthesizes the proposed gas-solid angular momentum balance model in a convenient form, taking advantage of the linear relationship between $\bar{\omega} r_b$ and v_{in}. The resistances have been separated according to their physical origin in such a way that the magnitude of $\bar{\omega} r_b$ decreases if any of the resistances increases.

4.2.4 Gas-only formulation

Equation (36) reduces to a gas-only formulation by considering $\bar{\rho} = \rho_g$ and $k = 1$. Additionally, $C_{f,ow}^{go}$ and $C_{f,ew}^{go}$ are the gas-only counterparts of the wall drag coefficients, and, as there is no solids bed, the lower limit of integration on **Equation (32)** is an arbitrary radius r with a corresponding circulation of $\Gamma_r = v_\theta r$. Equation 41 arises from all previous simplifications.

$$v_\theta r = \frac{v_{in}}{\frac{\frac{\alpha' C_{f,ow}^{go}}{I_0}}{\sqrt{1 + 2\frac{\alpha' C_{f,ow}^{go}}{I_0} cos\,\gamma\, R - 1}} + \frac{\alpha C_{f,ew}^{go}(R - r)}{I_0 L_R}} \tag{41}$$

Equation (41) correlates the average azimuthal gas velocity at radius r with the outer wall and end wall braking effects. The radius of analysis r must lie between the chamber radius R and the chimney radius r_{ch}. Angular resistances can still be derived for both walls, resulting in Equation 42 and Equation 43.

$$\mathcal{R}_{ow}^{go} = \frac{\alpha' C_{f,ow}^{go}}{I_0} \tag{42}$$

$$\mathcal{R}_{ew}^{go} = \frac{\alpha C_{f,ew}^{go}(R - r)}{I_0 L_R} \tag{43}$$

The Injection resistance $\mathcal{R}_{in}$, given by Equation 44, resembles its gas-solid definition in **Equation (37)**.

$$\mathcal{R}_{in}^{go} = \mathcal{R}_{in} = \frac{1}{cos\,\gamma\, R} \tag{44}$$

If $\mathcal{R}_{ow}^{go}$ tends to zero, the angular momentum balance on **Equation (41)** yields Equation 45.

$$v_\theta r = \frac{v_{in}}{\frac{1}{cos\,\gamma\, R} + \frac{\alpha C_{f,ew}^{go}(R - r)}{I_0 L_R}}$$

$$\Rightarrow v_\theta r = \frac{v_{in}}{\mathcal{R}_{in}^{go} + \mathcal{R}_{ew}^{go}} \tag{45}$$

Moreover, the condition $\mathcal{R}_{ew}^{go}$ tends to zero in **Equation (45)**, resulting in Equation 46.

$$\Rightarrow v_\theta r = v_{in}\, cos\,\gamma\, R \tag{46}$$

heeft opma
heeft opma
Cursief, Spel
heeft opma
heeft opma
Cursief, Spel
heeft opma
heeft opma
Cursief, Spel
heeft opma
heeft opma
Cursief, Spel
heeft opma

The latter corresponds to the angular momentum balance for a free vortex flow in vortex chambers [22]. Equation 47 describes how close the gas-only vortex flow is to a free vortex [27].

$$v_{in}\, cos\, \gamma\, R^m = v_\theta r^m \tag{47}$$

For $m = 1$ the flow behaves like a free vortex flow. It can be proven that $0 < m < 1$ for all possible values of **Equation** (41)~~(41)~~ in single-phase vortex chambers. Thus, the radial profile of the average azimuthal gas velocity in a single-phase flow will behave like a hyperbolic function with values strictly lower than its free vortex counterpart, in agreement with CFD simulations and experiments [28].

heeft opma
heeft opma
Cursief, Spel
heeft opma

However, gas-only flow behaves very differently from particulate flow, featuring distinct patterns such as near-wall jets [28], counterflows, backflows, gas bypass, cell flows [29], and non-stationary phenomena like the precessing vortex core [6]. In addition, the solids bed in a vortex chamber tends to smooth out and dissipate gas-phase phenomena [26], facilitating isotropy and symmetry assumptions such as those used in Section **4.1.**

4.2.5 Auxiliary equations

An auxiliary equation helps to close the nonlinear system of **Equations** (5)~~(5)~~ and (36)~~(36)~~. The output variables are the bed's average angular velocity $\bar{\omega}$, average bed's inner edge radius r_b, and average bed void fraction ε_g. For r_b, a proportionality between the bed's inner edge radius and the vortex chamber radius of the form $r_b = aR$ can be considered. However, this constant strongly depends on the set of operating conditions (v_{in}, M_s) and particle properties (d_p, ρ_s) as shown by different authors [18] [19]. Therefore, a more systematic approach is needed to describe the average bed's inner edge radius behavior for different design parameters and operating conditions.

heeft opma
heeft opma
Cursief, Spel
heeft opma
heeft opma
heeft opma
heeft opma

A radial force balance for the solids bed is the most straightforward alternative to this predicament. The two most dominating contributions of the solids bed force balance are the radially inwards drag force and the radially outwards solids bed centrifugal force, as stated by Kovacevic et al. [14] [18] and Fan et al. [30]. Equation 48 represents Newton's 2nd law for the center of mass of the solids bed.

$$F_{drag} = m_s \bar{a}_c \tag{48}$$

Every other dynamic and centrifugal force component that arises from a more rigorous formulation, such as the integral formulation by Fan et al. [30] and the differential formulation by Chen [31] for rotating fluidized beds (RFB), is demonstrably less than both of the previous forces by a factor of $\frac{\rho_g}{\rho_s}$, unless injection velocities and void fractions take very high or very low values, respectively. Thus, **Equation** (48)~~(48)~~ is a reasonable approximation for gas-solid centrifugal flows.

heeft opma
heeft opma
heeft opma

The location of interest for the radial force balance is the center of mass rather than the bed inner edge radius, as typically done in other formulations [11][18]. Newton's 2nd law formulation for equipollent force systems relies on the center of mass of the set of bodies

inside the control volume. Additionally, the rotating solids bed on a vortex chamber does not fluidize layer-by-layer like an RFB. Hence, the onset of centrifugal fluidization at the bed's inner edge radius could not be a valid fluidization criterion. Previous studies [1] [14] pointed out that vortex chambers feature different flow regimes compared with RFBs at the same centrifugal acceleration, with many intermediate and non-stationary states, which explains the need for more appropriate fluidization criteria. **Equation (48)~~(48)~~** is by no means a complete fluidization criterion; it only intends to model the behavior of the rotating solids bed when the drag force and centrifugal force exactly balance each other out, which, according to Gonzalez-Quiroga et al. and Kovacevic et al. [1] [14], is the lower bound required to achieve a uniformly distributed and stable solids bed. More research must be done regarding the most appropriate vortex chamber fluidization criteria.

Equation 49 gives the average centrifugal acceleration at the center of mass.

$$\bar{a}_c = \bar{\omega}^2 r_{cm} \tag{49}$$

The center of mass can be determined by assuming a homogenous solids bed of sufficient solids loading and gas injection velocity. Then, by applying centroid superposition for two circle sectors of angle α, one of radius R and one of radius r_b, to produce the vortex chamber cross-section (seen in **Figure 2~~Figure 2~~**), the resulting annular sector has a center of mass given by Equation 50.

heeft opma

$$r_{cm} = \frac{4\,sin\frac{\alpha}{2}}{3\alpha} * \frac{R^3 - r_b^3}{R^2 - r_b^2} \tag{50}$$

The interfacial gas-solid drag force F_{drag} is defined according to various models, each having its weaknesses and strengths. They can usually be written in the form of Equation 51.

$$\frac{F_{drag}}{V_b} = \beta\left|u_r - v_{r,sup}\right| \tag{51}$$

where β is the interphase momentum transfer coefficient, a function that depends entirely on the selected gas-solid drag model. Literature reports several analytical approaches using various drag models for radial force balance in vortex chambers. The Supplementary Material summarizes some of the most notable.

Of the entirety of drag models currently found in gas-solid vortex chamber literature, Gidaspow's model is, by a wide margin, the most prevalent of them. This prevalence is due, in part, to its simplicity and convergence properties in Euler-Euler CFD studies. Part of its ubiquity also comes from its wide range of applications, as it is the combination of Ergun's model for dense regimes ($\varepsilon_g < 0.80$) and Wen and Yu's model for dilute regimes ($\varepsilon_g > 0.80$) [5].

Most gas-solid drag models have been created for CFBs and packed beds and have been adapted or extended for their implementation in vortex chambers. An advantage of vortex chambers compared with CFBs is that solid beds of higher density and slip velocities can be

achieved [5]. Thus, it is more convenient to study vortex chambers in their most efficient operational context, i.e., on a relatively dense and uniformly distributed rotating solids bed with void fractions of much less than 0.8. Therefore, Ergun's drag model is selected to close the radial force balance on the proposed angular momentum model.

Equation 52 gives Ergun's interphase momentum transfer coefficient [5].

$$\beta_E = 150\frac{(1-\varepsilon_g)^2}{\varepsilon_g^2}\frac{\mu_g}{d_p^2} + 1.75\frac{(1-\varepsilon_g)\rho_g}{\varepsilon_g d_p}\left|u_r - v_{r,sup}\right| \tag{52}$$

Equation 53 results from neglecting radial solids displacement inside the vortex chamber.

$$u_r \cong 0$$

$$\Rightarrow \beta_E = 150\frac{(1-\varepsilon_g)^2}{\varepsilon_g^2}\frac{\mu_g}{d_p^2} + 1.75\frac{(1-\varepsilon_g)\rho_g}{\varepsilon_g d_p}v_{r,sup} \tag{53}$$

The gas radial superficial velocity at the center of mass is given by Equation 54.

$$v_{r,sup} = \frac{\dot{m}_g}{\varepsilon_g \rho_g \alpha r_{cm} L_R} \tag{54}$$

Substituting **Equation (4)~~(4)~~** in **Equation (54)~~(54)~~** yields Equation 55.

$$v_{r,sup} = \frac{I_0 v_{in}}{\varepsilon_g \alpha r_{cm}} \tag{55}$$

Equation 56 results from substituting **Equation (53)~~(53)~~** on **Equation (51)~~(51)~~**.

$$F_{drag} = \left[150\frac{(1-\varepsilon_g)^2}{\varepsilon_g^2}\frac{\mu_g}{d_p^2}v_{r,sup} + 1.75\frac{(1-\varepsilon_g)\rho_g}{\varepsilon_g d_p}v_{r,sup}^2\right]V_b \tag{56}$$

Then, substituting **Equations (49)~~(49)~~** and **(56)~~(56)~~** on **Equation (48)~~(48)~~** yields Equation 57.

$$\left[150\frac{(1-\varepsilon_g)^2}{\varepsilon_g^2}\frac{\mu_g}{d_p^2}v_{r,sup} + 1.75\frac{(1-\varepsilon_g)\rho_g}{\varepsilon_g d_p}v_{r,sup}^2\right]V_b = m_s\bar{\omega}^2 r_{cm} \tag{57}$$

By substituting **Equation (5)~~(5)~~**, we finally get Equation 58.

$$150\frac{(1-\varepsilon_g)^2}{\varepsilon_g^2}\frac{\mu_g}{d_p^2}v_{r,sup} + 1.75\frac{(1-\varepsilon_g)\rho_g}{\varepsilon_g d_p}v_{r,sup}^2 = (1-\varepsilon_g)\rho_s\bar{\omega}^2 r_{cm} \tag{58}$$

Equation (58)~~(58)~~ can now be solved simultaneously with **Equations (5)~~(5)~~** and **(36)~~(36)~~** for $\bar{\omega}$, ε_g, and r_b by using a nonlinear numerical solver for a set of known input parameters.

An alternative procedure can be done for any other radial drag model. In this case, there is a clear incentive to independently corroborate Ergun's drag model results, given its reported accuracy and physical significance deficiencies. This is advisable because, as seen in Ergun's original derivation [32], his model assumes a packed solids bed with little to no void fraction variations around $\varepsilon_g \approx 0.4$. This, according to Gibilaro [33], is not representative of typical expanded fluidized beds found in practice. The previous argument allowed him to propose a new model that included particle bed expansion in the gas pressure drop, using bed tortuosity and an expanded friction factor. Thus, following Gibilaro's original formulation, his model can be adapted to a vortex chamber, as shown in the Supplementary Material.

Although the previous formulations seem reasonable for typical vortex chambers, they are not universally valid. For instance, **Equation** (48)~~(48)~~ is not always valid for low solids loading or very high gas injection velocities. Under these conditions, the centrifugal force becomes greater than the radial drag force, meaning the outer wall and end wall contact forces become much more considerable and significantly influence the radial force balance. Furthermore, radial-force-balance models disregard the particles' radial deflection at the gas injection, which could result in non-negligible radial solids velocities, radial impingement forces, and end wall contact forces in specific regions of the vortex chamber. Hence if experimental information about the void fraction or bed's inner edge radius is available, it is strongly suggested to use that data instead. The auxiliary equations can be implemented whenever there is insufficient input data while exercising caution regarding the physicality of void fraction and bed edge radius results.

Graphs of correlations between relevant variables and other significative results are shown in Section **5.1** for two different auxiliary equations, where applicable: Ergun's drag model, and the ratio $r_b = aR$ fitted to a relevant point of operation.

5 RESULTS AND DISCUSSION

5.1 Model Validation

The proposed angular momentum model for vortex chambers has been validated using datasets from three investigations, as described in Table 1~~Table 1~~. Niyogi et al. [19] comprise experimentally validated Euler-Euler CFD simulation of 1g-Geldart B- and D-type particles on a 54 cm diameter vortex chamber with an L/D aspect ratio of 0185. Kovacevic et al. [18] consist of experimental measurements of 1g-Geldart B-type and D-type particles on a 54 cm diameter in a vortex chamber with an L/D aspect ratio of 0185. Finally, Gonzalez-Quiroga et al. [1] consist of experimental measurements of 1g-Geldart B-type particles on an 8 cm diameter vortex chamber with an L/D aspect ratio of 0187.

An exploration of the current state of the art on vortex chambers research returns only a handful of investigations that correlate multiple relevant operating conditions for the cold flow hydrodynamics and provide sufficient input/output data to make meaningful predictions. In particular, radial profiles for the average or the maximum particle azimuthal velocity were instrumental in acquiring sufficient information about the solids bed, which resulted in realistic values of predicted bed heights and bed voidage, and also fitted C_f values

of good confidence, according to relevant literature [11][21]. All three investigations in Table 1 report radial profiles of multiple hydrodynamic variables, while only Gonzalez-Quiroga et al. reports azimuthal and radial profiles.

The proposed angular momentum balance model has three degrees of freedom: k, $C_{f,ow}$, $C_{f,ew}$. However, only one degree of freedom fits the data for validation purposes. A decision was made to fix $k = 0.1$ based on Anderson et al. [11] and to merge the outer wall and end wall drag coefficients into one as $C_f = C_{f,ow} = C_{f,ew}$ following Smulsky's procedure [13]. This will not restrict the model's effectiveness considerably, given that the model output variables $(\bar{\omega}, \varepsilon_g, r_b)$ depend weakly on the expansion factor k, as shown in Section **5.2**. However, we expect very different behaviors between the outer wall and end wall drag coefficients, so the decision to implement an "effective" drag coefficient C_f that coalesces both boundary effects into one number is only provisional and for comparison purposes. Subsequent investigations will address k, $C_{f,ow}$ and $C_{f,ew}$ in a more direct, systematic approach. The model enables the calculation of the radially-averaged azimuthal velocity of the solids bed by considering the linear velocity profile of the rigid body-like rotation, as indicated in Equation 59.

$$\bar{u}_{\theta_{\bar{r}}} = \bar{\omega}_s \left(\frac{R + r_b}{2} \right) \tag{59}$$

Table 1~~Table 1~~ shows the points of operation used to fit the merged wall-bed drag coefficient C_f. The rest of the aggregated data serves for validating and assessing the model and can be found in the respective bibliography.

heeft opma

Table 1 Datasets. Only the points of operation used to fit the model are shown.

Datasets	**Gonzalez-Quiroga et al.** [1]		**Kovacevic et al.** [18]			**Niyogi et al.** [19]	
R, mm	40		270			270	
L_R, mm	15		100			100	
l_0, mm	0.94		2			2	
I_N	8		36			36	
$\gamma, °$	10		10			10	
Fluid	Air @ 20 °C and 1 atm		Air @ 15 °C and 1 atm			Air @ 15 °C and 1 atm	
$\rho_g, kg\ m^{-3}$	1.204		1.225			1.225	
$\mu_g, kg\ m^{-1}\ s^{-1}$	$1.789 * 10^{-5}$		$1.813 * 10^{-5}$			$1.813 * 10^{-5}$	
Solids	Aluminum particles	Walnut shells	HDPE (multiple d_p)	HDPE (multiple M_s)	HDPE and Polycarbonate	Multiple densities	Multiple d_p
$\rho_s, kg\ m^{-3}$	2700	700	950	950	(950; 1240)	(450;	950

						950; 1800)	
d_p, mm	0.5	0.53	(1; 1.5; 2)	1.5	2	1	(0.5; 2)
M_s, kg	$10.7 * 10^{-3}$	$7.88 * 10^{-3}$	2	(3; 4; 5.4)	(5.5; 5.8)	2	2
$v_{in}, m\ s^{-1}$	91.38	92.15	70	70	100	54.17	54.17
$\bar{u}_{\theta\bar{r}}, m\ s^{-1}$	2.00	3.59	(7.78; 6.16; 5.41)	(6.45; 6.10; 5.14)	(6.24; 4.22)	(6.60; 5.84; 4.29)	(7.45; 4.08)

5.1.1 Niyogi et al. data

Niyogi performed a parametric study for various gas inlet velocities and particle properties, such as average solids density and average particle diameter. However, because the angular momentum model has one degree of freedom, the merged wall-bed drag coefficient must be fitted to one data point. Therefore, the validation dataset consists of average solids bed azimuthal velocity measurements for 2 kg of 1 mm HDPE particles and different inlet gas velocities, ranging from 18.94 m/s to 109.24 m/s, as shown in Figure 6~~Figure 6~~.

heeft opma

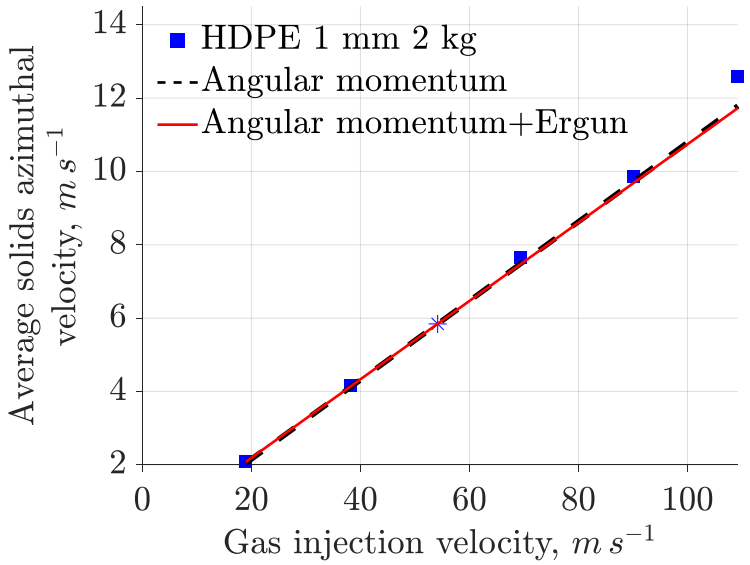

Figure 6 Gas injection velocity vs. Average solids azimuthal velocity for 1 mm 2 kg HDPE particles. The asterisk corresponds to the fitted point.

All three models were fitted to the third data point, enumerated from left to right, corresponding to an inlet velocity of $54.17\ m/s$. This produces a C_f value of $3.78 * 10^{-3}$

for Ergun's model. Concerning the average void fraction, Ergun's model returned a value of 0.5002 at the fitted point.

Additionally, Niyogi et al. provided enough experimental data to extract the ratio $\frac{r_b}{R} = 0.9037$ at the fitted point. Using this ratio, the proposed angular momentum model could be implemented without any auxiliary equation, shown in **Figure 6**~~**Figure 6**~~ as a black dashed line. This model produced an average bed voidage of 0.4986. Considering that the experimental average void fraction provided by Niyogi et al. at the fitted condition is 0.5250, the relative error for Ergun's model is 4.7%.

Concerning the average bed height, Ergun's model returned 26.10 mm at the fitted point. The experimental average bed height provided by Niyogi et al. at the fitted condition is reported to be 26.00 mm. Thus, the relative error of Ergun's model is 0.38%. This result and the average void fraction relative errors indicate that Ergun's model is suitable to describe vortex chamber beds similar to the ones studied by Niyogi et al.

Lastly, one can see from **Figure 6**~~**Figure 6**~~ that the two models follow the data points very closely. This result seems to imply that, if everything else stays equal, C_f is virtually constant for the studied range of gas injection velocities. This range of no correlation between the wall-bed drag coefficient and the gas injection velocity may correspond to the region where the gas-solid drag force is roughly proportional to the gas injection velocity, predicted by de Wilde and de Broqueville [5] and observed experimentally by Rosales-Trujillo et al. [20] and Gonzalez-Quiroga et al. [1]. For greater injection velocities, the inlet gas angular momentum may be too high to be transferred efficiently to the bed, so the assumptions of a stable axisymmetrical rotating solids bed or the azimuthal no-slip condition at the bed's inner edge may not hold. As will be seen in subsequent sections, the invariant property of the wall-bed drag coefficient C_f with respect to gas injection velocity will prove instrumental for scale-up purposes.

Figure 7~~**Figure 7**~~ shows a parity plot to evaluate the models' fitness relative to the measured azimuthal velocities of solids by Niyogi et al.

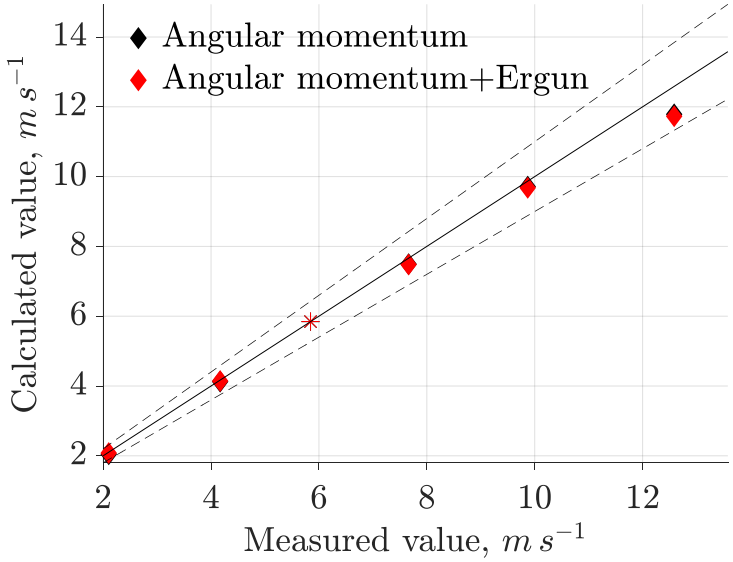

Figure 7 Parity plot for the average solids azimuthal velocity for 1 mm 2 kg HDPE particles. The asterisks are the fitted data points. The dashed lines represent a ±10% margin of error.

Regarding **Figure 7**~~**Figure 7**~~, the rightmost data point yields a relative error of -6.80% for the two models, while the rest produce relative errors of less than $\pm$2.4%. Thus, the two models produce virtually identical results, with the highest standard deviation being 0.024 for the rightmost data point. The deviation of this data point, corresponding to an inlet gas velocity of 109 m/s, may be related to the overestimation of the wall-bed braking effect in the angular momentum model.

Niyogi et al. provided more usable data than the one employed here for validation. These extra datasets are in the form of radial profiles of the average solids azimuthal velocity for a specific variation in solids parameter, all at the same inlet gas velocity of $54.17\,m/s$. However, no other invariant quantity (other than the inlet gas velocity itself) could be determined from these variations. Thus, no parity plots could be constructed from them, given that each new data point would need to be used to fit each merged wall-bed drag coefficient C_f. Nonetheless, the fitted C_f values are of great importance and have been calculated in **Table 2**~~**Table 2**~~ using Ergun's model.

Table 2 Fitted C_f values for various datapoints extracted from Niyogi et al. [19]*, using the developed angular momentum model and Ergun's radial drag model.*

Solid particles	Fitted C_f value, $*\,10^{-3}$
For 2 kg of 0.5 mm particles of 950 kg/m^3	2.94
For 2 kg of 1 mm particles of 450 kg/m^3	4.58
For 2 kg of 1 mm particles of 950 kg/m^3	3.78

For 2 kg of 1 mm particles of 1800 kg/m^3	4.81
For 2 kg of 2 mm particles of 950 kg/m^3	5.61

5.1.2 Kovacevic et al. data

Kovacevic et al. produced a wide arrange of experimental data parallel to the CFD simulations by Niyogi et al., which have been divided here into subsets according to the experimental design. The experimental results enable us to account for all variables relevant to the angular momentum model. Thus, significant correlations can be inferred between the average solids azimuthal velocity at different solids loadings, particle diameters, and particle densities, all at distinct inlet gas velocities in the range of 55 m/s to 110 m/s.

Since Kovacevic et al. only reported maximum solids azimuthal velocity values and some radial profiles for the solids azimuthal velocity. The Supplementary Material describes the data post-processing procedure to find the average solids azimuthal velocity required to validate the angular momentum model.

5.1.2.1 For different solids loadings

This dataset corresponds to average solids azimuthal velocity measurements of 1.5 mm particles HDPE (950 kg/m^3) at different inlet gas velocities for three different solids loadings. The 5.4 kg solids loading corresponds to the maximum solids loading for HDPE 1.5 mm particles for this vortex chamber, as stated by the authors [18]. The models were fitted to the second injection velocity of 70 m/s, enumerated from left to right, featured in **Figure 8**~~**Figure 8**~~.

heeft opma

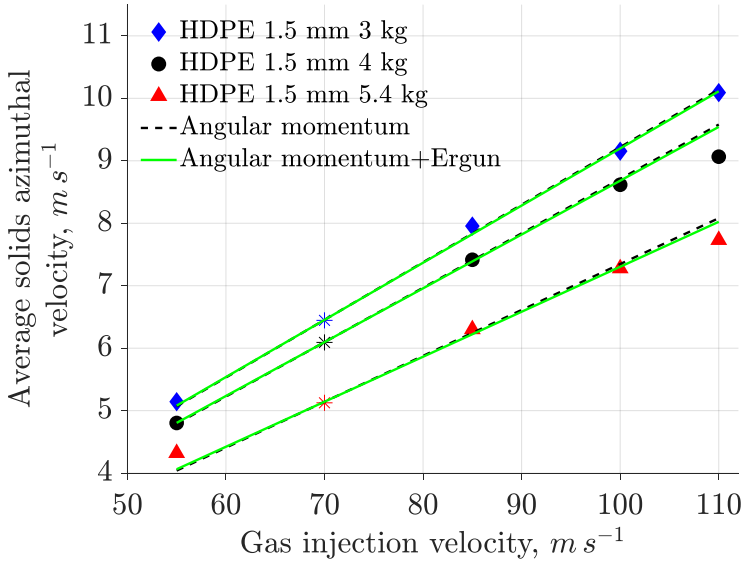

Figure 8 Gas injection velocity vs. Average solids azimuthal velocity for 1.5 mm HDPE for different solids loadings and gas injection velocities. The asterisks correspond to the fitted points.

Table 3~~Table 3~~ presents the wall-bed drag coefficients fitted for each solids loading.

Table 3 Fitted wall-bed drag coefficients for different solids loadings for the dataset of Kovacevic et al.

Solids loading, kg	Fitted C_f value, $* 10^{-3}$
	Ergun's model
3	3.25
4	2.88
5.4	3.27

Here the angular momentum model and the angular momentum combined with the radial drag model are not truly independent. Kovacevic et al. only gave information about bed edge radii for three solids loadings at a gas injection of 110 m/s. The bed edge radius does vary significantly for different gas injection velocities, so it could not be used to find an independent expression for $\frac{r_b}{R}$ at the fitted point. Instead, it was fitted using the predicted bed edge radius from Ergun's model.

Table 4 Predicted average void fraction for different solids loadings for the dataset of Kovacevic et al.

Solids loading, kg	Average void fraction
	Ergun's model
3	0.4723
4	0.4935

5.4	0.5581

Table 5 Predicted average bed height for different solids loadings for the dataset of Kovacevic et al.

Solids loading, kg	Average bed height, mm
	Ergun's model
3	37.94
4	54.51
5.4	91.24

The predictions for average bed voidage and average bed heights for different solid loadings are given in Table 4~~Table 4~~ and Table 5~~Table 5~~, respectively. These results are well within reason, given that an increase in solids loading should be accompanied by an increase in bed voidage and bed height if the injection velocity stays constant.

heeft opma

heeft opma

Lastly, a particular non-monotonic relationship between the solids loading and C_f can be seen to develop. A suspected C_f local minimum appears for a solids loading of 4 kg for Ergun's radial drag model. This minimum could be a striking feature since minimizing wall-bed drag coefficients would maximize the average solids azimuthal velocity and average solids bed centrifugal acceleration and, in turn, benefit specific vortex chamber processes and the overall PI potential. However, more data is needed to locate this local minimum properly.

The parity plots for all three solids loadings are virtually identical, as shown in Figure 9~~Figure 9~~.

heeft opma

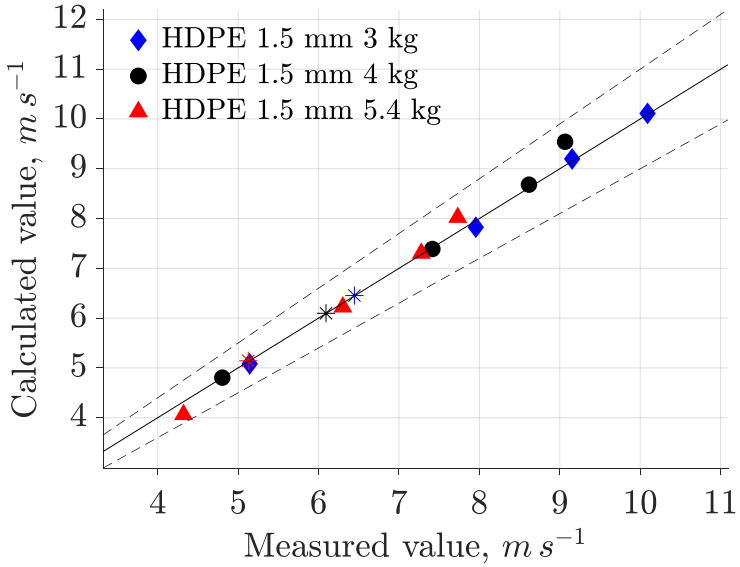

Figure 9 Parity plot for the average solids azimuthal velocity for 1.5 mm HDPE particles. The asterisks are the fitted data points. The dashed lines represent a ±10% margin of error.

Regarding Figure 9~~Figure 9~~, the relative errors for the average solids azimuthal velocity lie in the range of -5.98% and 5.26% for all three solids loadings. One can see that the last data points on each subset tend to produce more positive relative errors. A plausible explanation comes from what happens after surpassing the linear proportionality region between the inlet gas velocity and the average solids azimuthal velocity. Typically, further increases in inlet gas velocity after this region produce diminishing returns in solids azimuthal velocities, as observed by Gonzalez-Quiroga et al. [1] and Rosales-Trujillo et al. [20], until reaching a certain plateau where if the inlet gas velocity is increased further only marginal gains in the solids azimuthal velocity will be observed. Additionally, this is more apparent for heavier beds, suggesting a correlation between gas injection velocity and solids loading with the angular momentum transfer efficiency between the incoming gas and the solids bed.

5.1.2.2 For different particle diameters

This dataset corresponds to average solids azimuthal velocity measurements of 2 kg of HDPE particles ($950\ kg/m^3$) at different inlet gas velocities for three different particle diameters. Since the bare angular momentum model does not consider the particle diameter by itself, it cannot be validated by this dataset nor discern any meaningful relationship. Therefore, the angular momentum model will only be considered with Ergun's radial drag model. The model was fitted to the second injection velocity of $70\ m/s$, enumerated from left to right, featured in Figure 10~~Figure 10~~.

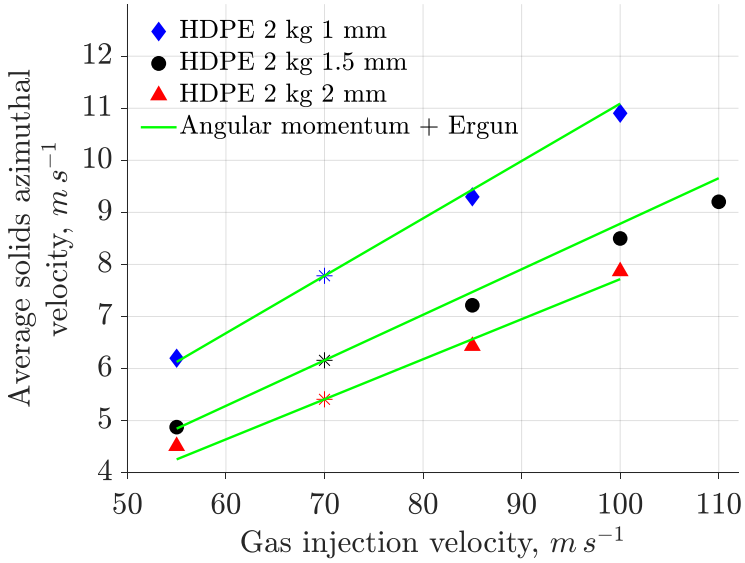

Figure 10 Gas injection velocity vs. Average solids azimuthal velocity for 2 kg of HDPE for different particle diameters and gas injection velocities. The asterisks correspond to the fitted points.

Table 6 Fitted wall-bed drag coefficients for different particle diameters for the dataset of Kovacevic et al.

Particle diameter, mm	Fitted C_f value, $* 10^{-3}$
	Ergun's model
1	3.6333
1.5	4.7257
2	5.4358

Table 6~~Table 6~~ presents the wall-bed drag coefficients fitted for each particle diameter. A monotonically increasing tendency is evident on C_f for Ergun's model. This tendency is aligned with the notion that bigger particles tend to produce more stable, although slower, rotating beds according to their Stokes number.

heeft opma

Table 7 Predicted average void fraction for different particle diameters for the dataset of Kovacevic et al.

Particle diameter, mm	Average void fraction
	Ergun's model
1	0.4834
1.5	0.4838
2	0.4745

Table 8 Predicted average bed heights for different particle diameters for the dataset of Kovacevic et al.

Particle diameter, mm	Average bed height, mm
	Ergun's model
1	25.20
1.5	25.22
2	24.75

The predictions for average bed voidage and average bed heights for different particle diameters are given in Table 7~~Table 7~~ and Table 8~~Table 8~~, respectively. These findings agree with Niyogi et al. [19], who found the same bed height and voidage behavior as predicted here. Their simulations hardly changed the bed height for different particle diameters at the same solids loading. Conversely, the bed tends to be bubbly and diffuse for lower particle diameters, so identifying the bed edge radius becomes much more complicated.

heeft opma

heeft opma

The parity plot for Ergun's radial drag model is shown in Figure 11~~Figure 11~~.

heeft opma

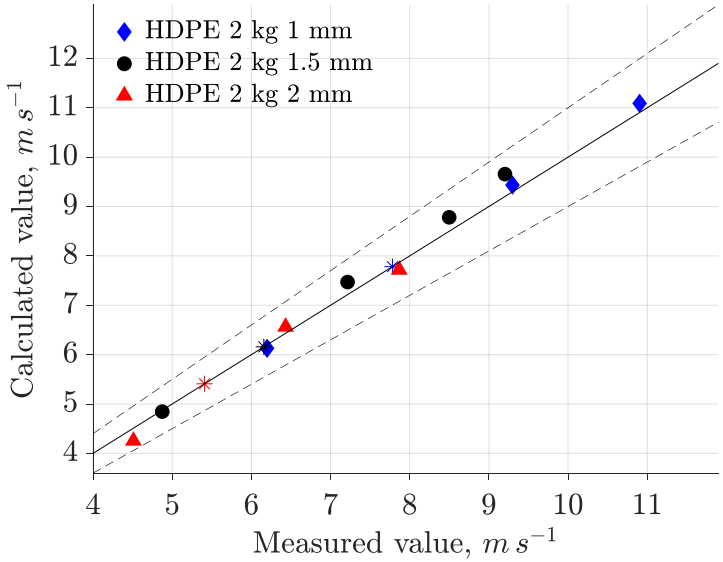

Figure 11 Parity plot for the average solids azimuthal velocity for 2 kg of HDPE particles. The asterisks are the fitted data points. The dashed lines represent a ±10% margin of error.

Regarding **Figure 11**~~**Figure 11**~~, the relative errors for the average solids azimuthal velocity lie in the range of -5.66% and 4.92%. Kovacevic et al. also provided two radial profiles for two different particle densities of 2 mm particles at the maximum solids loading allowed for these conditions. The solids in question are HDPE ($950\ kg/m^3$) and PC ($1240\ kg/m^3$) and their maximum solids loadings are 5.5 kg and 5.8 kg, respectively. Since they only provided radial profiles for a set of parameters not coincident with any of the previous datasets, no relationship C_f vs. v_{in} nor parity plot can be constructed. However, the two fitted C_f values are given here for reference in **Table 9**~~**Table 9**~~ using Ergun's model.

Table 9 Fitted C_f values for two datapoints extracted from Kovacevic et al. [18]*, using the developed angular momentum model and Ergun's radial drag model.*

Solid particles	Fitted C_f value, $* 10^{-3}$
For 5.5 kg of 2 mm particles of $950\ kg/m^3$	3.8594
For 5.8 kg of 2 mm particles of $1240\ kg/m^3$	5.7500

5.1.3 Gonzalez-Quiroga et al. data

The work of Gonzalez-Quiroga et al. contains average azimuthal velocity data for two different particles at various solids loadings and injection velocities. The solid particles in question are crushed walnut shells ($0.53\ mm, 700\ kg/m^3$) and monodispersed aluminum spheres ($0.5\ mm, 2700\ kg/m^3$) both of which classify as 1g-Geldart B-type particles. These particle properties, coupled with a relatively small chamber diameter (80 mm) and high injection velocities in the range of $82\ m/s$ and $126\ m/s$, produce relatively dense and uniform rotating solids beds.

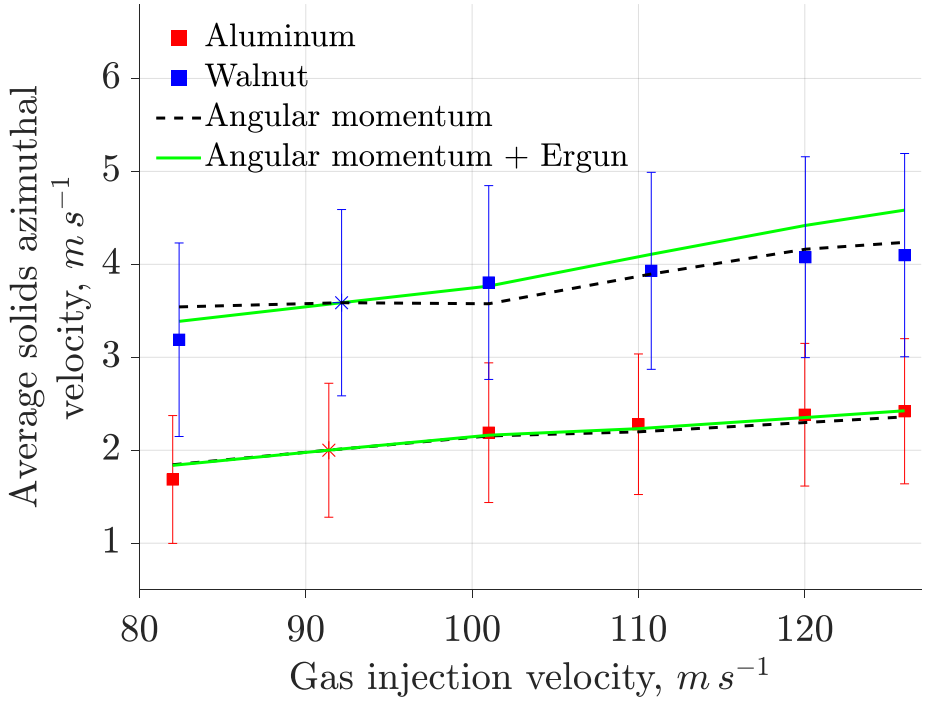

Figure 12 Gas injection velocity vs. Average solids azimuthal velocity for Aluminum spheres and Walnut shells at different solids loadings and gas injection velocities. The error bars correspond to twice the standard deviation from 3 measurements by Gonzalez-Quiroga et al. The asterisks correspond to the fitted points.

Both models were fitted to their second injection velocity, enumerated from left to right, as shown in **Figure 12**~~**Figure 12**~~. These conditions correspond to (91.38 m/s, 10.7 g) for aluminum spheres and (92.15 m/s, 7.88 g) for walnut shells, respectively. This dataset is particular because each datapoint corresponds to a different solids loading and inlet gas velocity. According to Gonzalez-Quiroga et al. [1], the error bars correspond to twice the standard deviation of the experimental data. At the same time, all three models predict azimuthal velocity values well within that range.

Table 10~~**Table 10**~~ shows the wall-bed drag coefficients at the fitted points. These values are certainly higher than the ones obtained for the other datasets, which implies a correlation between C_f and certain parameters of this dataset. This correlation will be explored further in Section **5.3**.

Table 10 Fitted wall-bed drag coefficients for aluminum spheres and walnut shells for the dataset of Gonzalez-Quiroga.

Solid particles	Fitted C_f value, $* 10^{-3}$
	Ergun's model
Aluminum spheres ($10.7\ g, 0.5\ mm, 2700\ kg/m^3$)	8.53

Walnut shells ($7.88\ g, 0.53\ mm, 700\ kg/m^3$)	7.92

Table 11 Predicted average void fractions for aluminum spheres and walnut shells for the dataset of Gonzalez-Quiroga.

Solid particles	Average void fraction
	Ergun's model
Aluminum spheres ($10.7\ g, 0.5\ mm, 2700\ kg/m^3$)	0.5651
Walnut shells ($7.88\ g, 0.53\ mm, 700\ kg/m^3$)	0.5943

The predictions for average bed voidage for aluminum spheres and walnut shells are given in **Table 11**~~Table 11~~. According to Gonzalez-Quiroga et al., the void fractions for aluminum and walnut particles for an injection velocity of 101 m/s are 0.70 and 0.79, respectively. Although the models correctly predict walnut shells having a greater void fraction than aluminum spheres, the prediction error is too large. This discrepancy may stem from the invalidity of the radial drag formula on **Equation** **(48)**~~(48)~~ for the set of parameters and conditions of this dataset, possibly due to the small chamber radius or that the two solid particles considered are 1g-Geldart B-type.

heeft opma

heeft opma

heeft opma
Cursief, Spel

heeft opma

Gonzalez-Quiroga et al. reported radially and azimuthally averaged solids azimuthal velocities instead of radially averaged solids azimuthal velocities at an arbitrary azimuthal angle. The latter method corresponds to the one used by Kovacevic et al. and Niyogi et al., which could cause some comparison issues if the gradients in the azimuthal direction are too large. However, both groups of authors assure that their rotating beds are dense and uniformly distributed, so these gradients should be sufficiently low.

Table 12 Predicted average bed heights for aluminum spheres and walnut shells for the dataset of Gonzalez-Quiroga.

Solid particles	Average bed height, mm
	Ergun's model
Aluminum spheres ($10.7\ g, 0.5\ mm, 2700\ kg/m^3$)	2.494
Walnut shells ($7.88\ g, 0.53\ mm, 700\ kg/m^3$)	8.201

Table 12~~Table 12~~ shows the predictions for average bed height for aluminum spheres and walnut shells. The experimental average bed heights for aluminum and walnut particles are around 4 mm and 6 mm, respectively [1]. Thus, the predicted average bed heights are also off from the experimental values, an outcome expected by the intimate relationship between the average bed height and the average void fraction in the angular momentum model. The parity plots for both models are virtually identical, as shown in **Figure 13**~~Figure 13~~.

heeft opma

heeft opma

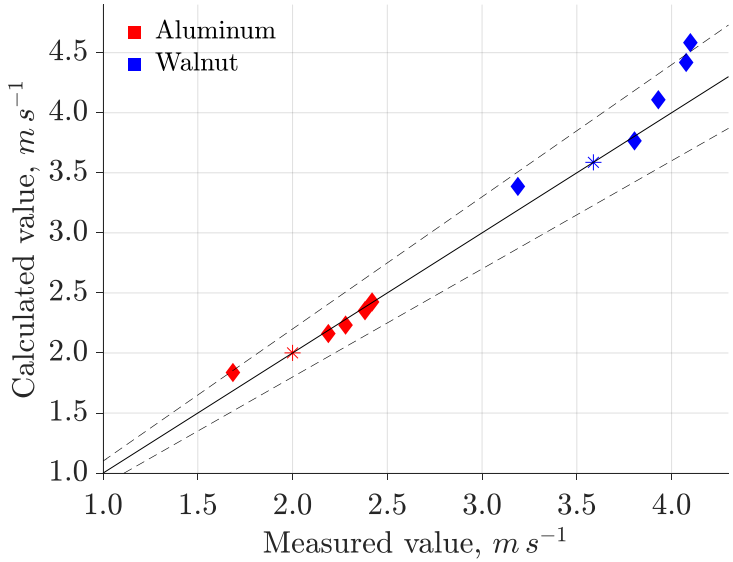

Figure 13 Parity plot for the average solids azimuthal velocity for aluminum spheres and walnut shells at various solids loadings and gas injection velocities. The dashed lines represent a ±10% margin of error.

Regarding **Figure 13**~~**Figure 13**~~, the relative errors for the average solids azimuthal velocity lie in the range of -2.1% and 9.0% for aluminum spheres, while in the range of -1.0% and 11.8% for walnut shells. Thus, the model exhibits a relatively high dispersion in its predictions for walnut shells, while it appears reasonably accurate for aluminum spheres. It can be surmised that the walnut shells rotating beds are beyond the linear proportionality region between the inlet gas velocity and the average azimuthal velocity of particles, possibly due to their relatively low solid density and Stokes number. On the other hand, aluminum rotating beds seem entirely predictable still, possibly due to their higher solid density and, thus, higher Stokes number.

5.1.4 Full parity plot

A parity plot containing all the predicted values, excluding the fitted pairs, is shown in **Figure 14**~~**Figure 14**~~. The angular momentum model with a coupled radial drag model is robust enough to analyze and predict rotating solids beds in vortex chambers, including diverse particle types, chamber design, and hydrodynamic conditions, responding well within acceptable engineering tolerances.

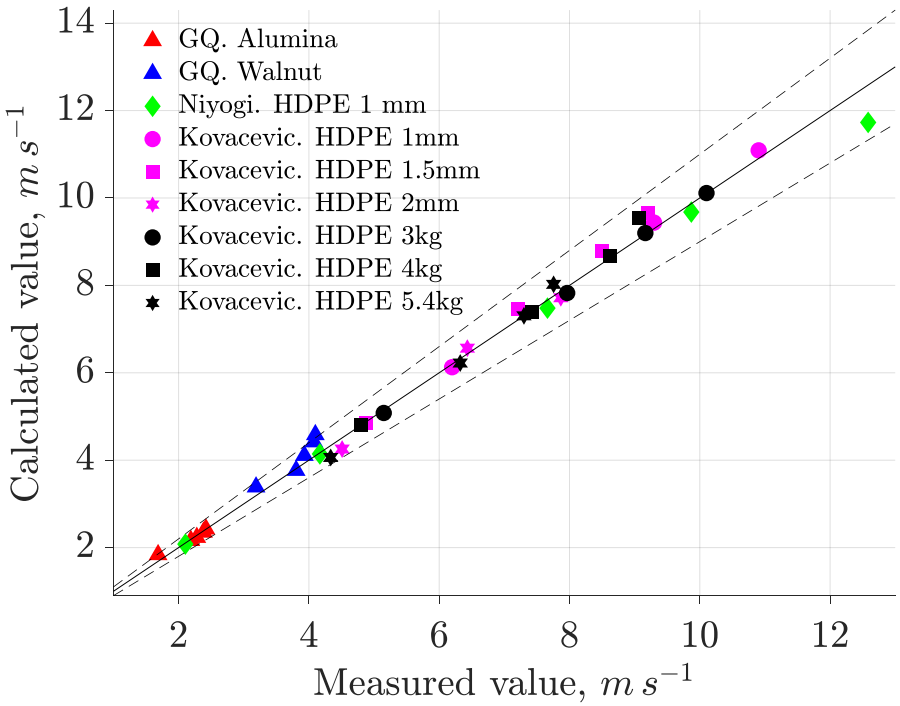

Figure 14 Parity plot for the average solids azimuthal velocity for all studied datasets. The studied range covers average solids azimuthal velocities from 1 m/s to 13 m/s. The dashed lines represent a ±10% margin of error.

5.2 Sensitivity analysis

Figure 15~~**Figure 15**~~ shows the complete sensitivity analysis for the dataset of Niyogi et al., with the implementation of Ergun's radial drag model.

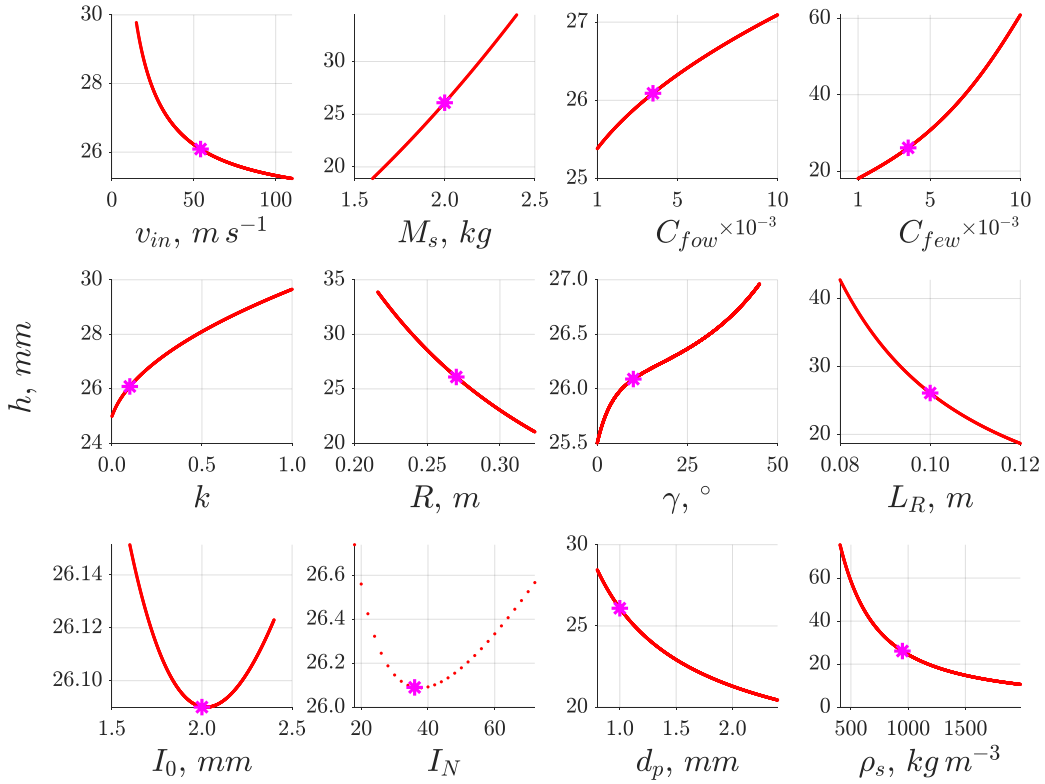
h, mm
v_in, m s^-1
M_s, kg
C_fow ×10^-3
C_few ×10^-3
k
R, m
γ, °
L_R, m
I_0, mm
I_N
d_p, mm
ρ_s, kg m^-3

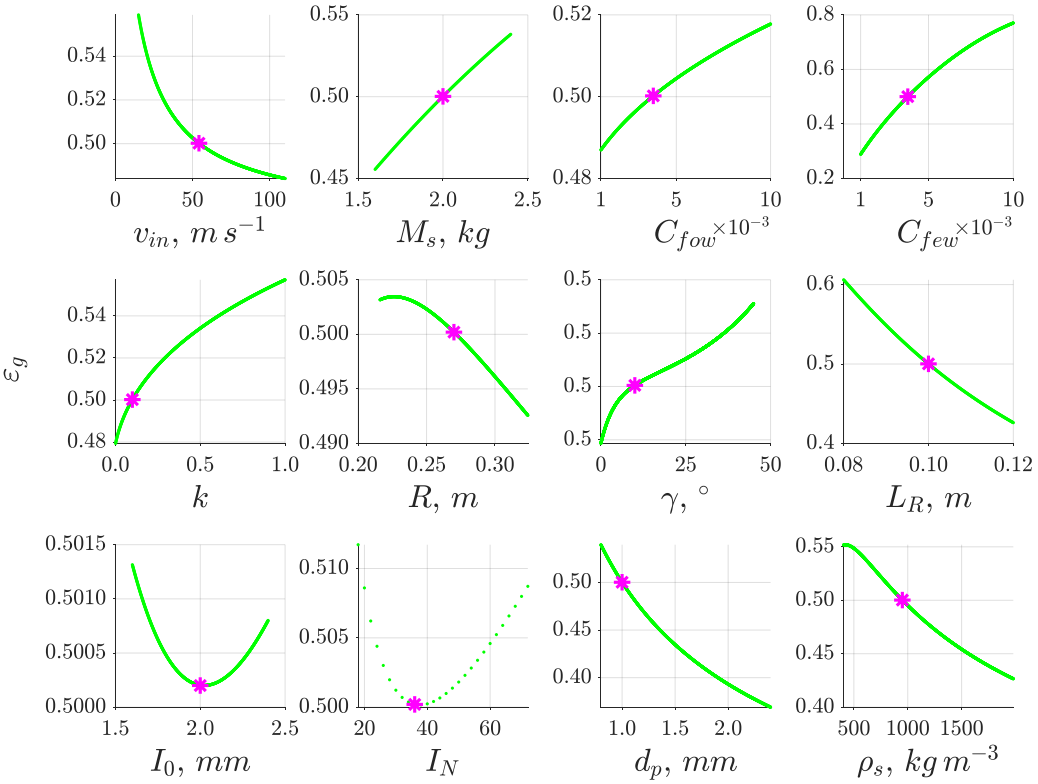
ε_g
v_{in}, $m\,s^{-1}$
M_s, kg
C_{fow} $\times 10^{-3}$
C_{few} $\times 10^{-3}$
k
R, m
γ, $^\circ$
L_R, m
I_0, mm
I_N
d_p, mm
ρ_s, $kg\,m^{-3}$

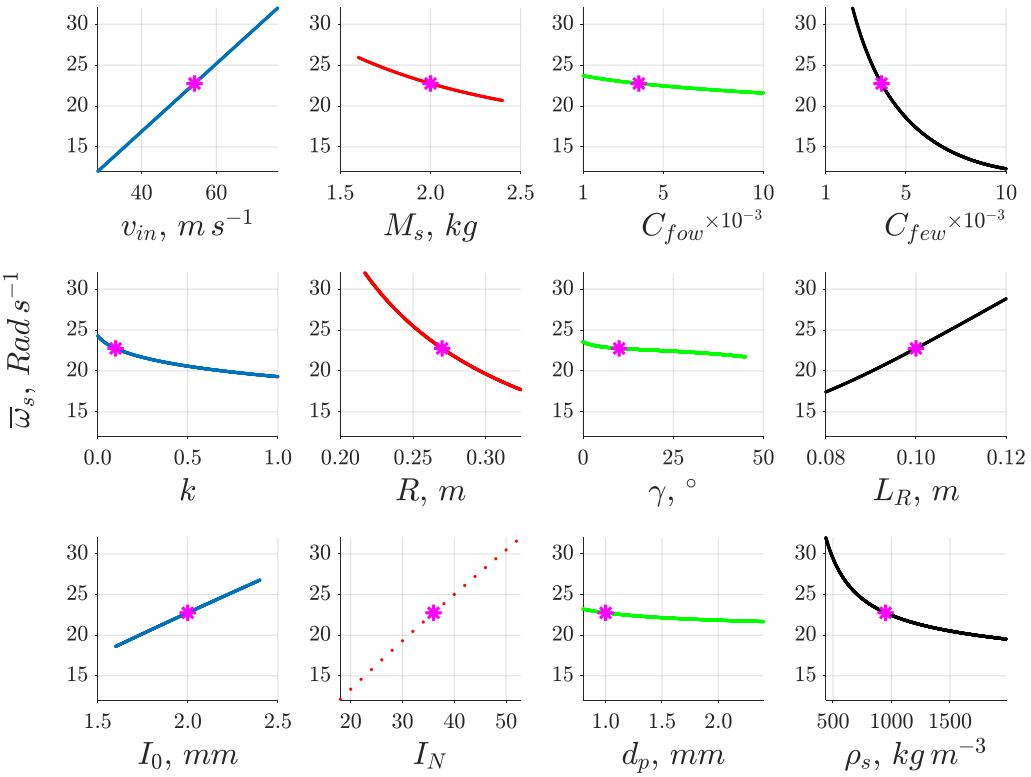

Figure 15 Sensitivity analysis of the average bed height, average void fraction, and average solids angular velocities for ceteris paribus changes to each input variable. The asterisks are the fitted data point.

The domain of each variable is limited to the immediate vicinity of the experimental data of Niyogi et al. for a rotating solids bed of HDPE particles; average particle diameter of 1 mm; solids loading of 2 kg; inlet gas velocity of 54.17 m/s; merged wall-bed drag coefficient of $3.7806 * 10^{-3}$; average bed height of 26.10 mm; and average solids azimuthal velocity of 5.84 m/s (See **Table 1**~~**Table 1**~~).Table 1 Datasets. Only the points of operation used to fit the model are shown~~Table 1 Datasets. Only the points of operation used to fit the model are shown~~. Variations of around $\pm 20\%$ of the reference value are induced to each variable in a *ceteris paribus* fashion, only evaluating states close to the variable's original stationary value and assuming the other variables stay constant. One can observe from **Figure 15**~~**Figure 15**~~ the following tendencies relative to the solids bed average angular velocity $\overline{\omega}_s$:

- A monotonically increasing trend for v_{in}, L_R, I_0, and I_N.
- A monotonically decreasing trend for M_s, $C_{f,ow}$, $C_{f,ew}$, k, R, γ, d_p, and ρ_s.

These qualitative findings are all in accordance with previous research [11][14][18][19] [25][34][35][36]. Notably, increasing the value of the chamber design parameters L_R, I_0, I_N implies a greater gas mass flow rate while maintaining a constant inlet velocity. This, of

course, also increases the inlet gas angular momentum and produces faster and denser beds, as expected.

Using Gibilaro's drag model instead of Ergun's produces similar trends as the ones shown here, though predicting, on average, more compact and shallow rotating beds than Ergun's model, as said before.

The angular momentum model can also offer insight into the sensitivity of $\bar{\omega}_s$ to perturbations in hydrodynamic variables and design parameters. Figure 15~~Figure 15~~ shows that marginal changes in $C_{f,ew}$ produce large variations in $\bar{\omega}_s$; and that marginal changes in $C_{f,ow}$ produce relatively small variations in $\bar{\omega}_s$. Figure 16~~Figure 16~~ illustrates this situation from a more global perspective.

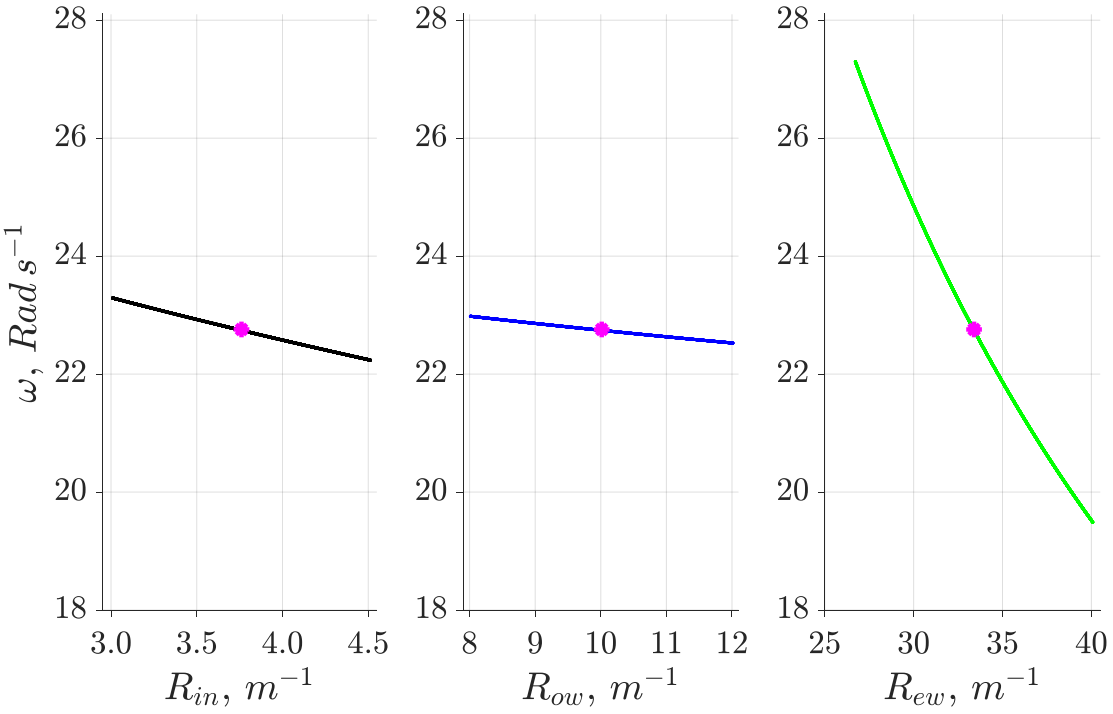

Figure 16 Sensitivity analysis for angular resistances for ceteris paribus changes to each of them.

Figure 16~~Figure 16~~ reveals that end wall braking effects on the solids bed are around one order of magnitude greater than the outer wall and gas injection, according to the proposed angular momentum model. Such bias is covered by Smulsky [13], who describes the characteristic flow pattern as "weighted rotated layers": a flow pattern where the end walls of the vortex device take a more prominent role in the solids bed development in comparison to the outer wall-centric "rotated layers", more appropriate for cyclonic devices instead. This disproportion between $\mathcal{R}_{ew}$ and $\mathcal{R}_{ow}$ can be potentially exploited by applying the Pareto principle to the improvement and enhancement of conventional vortex chamber design,

considering first and foremost the optimization alternatives that promote a reduction in $\mathcal{R}_{ew}$ over the other alternatives.

Remarkably, the same qualitative tendencies presented in this section arise for Kovacevic et al. and Gonzalez-Quiroga et al. experiments, which is proof of the consistency and well-behavior of the angular momentum balance model. The numerical assumption of the expansion factor at the gas injection k being equal to 0.1 does change the absolute value of the outer wall resistance $\mathcal{R}_{ow}$, but, as seen in **Figure 15**~~**Figure 15**~~, the solids bed average velocity is minimally affected by its value. Nevertheless, the actual value of the outer wall drag coefficient $C_{f,ow}$ should be very sensitive to k's value, so a more appropriate way to determine the expansion factor at the gas injection k for a broad variety of vortex chamber parameters and operating conditions should be developed.

5.3 Wall-bed drag coefficient analysis

The proposed angular momentum balance model contains the following improvement opportunities:

- The model does not consider the hydrodynamic effects caused by variations in the chimney's and end walls' geometry. This is relevant for beds composed of finer solid particles, such as 1g-Geldart A- and C-type particles, which are considerably more sensitive to the chimney's dimensions and typology than coarser particle beds. Fine particle beds in a vortex chamber are typically rarefied and non-homogeneous, with no clear bed edge [18] and, generally, low Stokes numbers. These conditions promote a more fluid-like behavior and, thus, a propensity to be affected and entrained by the vortex core and both the chimney's and end walls' low-pressure zones and near-wall jet phenomena. Nevertheless, the case is not the same for 1g-Geldart D- and B-type particles, given that these particles produce relatively dense and uniformly distributed beds. Therefore, the freeboard pressure drop could be modeled with Volchkov's model of hydraulic resistances [37]. Additionally, the thickness of the outlet gas annular flow through the chimney could be modeled via Goldshtik's minimal outgoing kinetic energy flux rule [6].
- The model does not consider non-conventional variations in the geometry and configuration of inlet gas slits, with possibly a few exceptions (see Section **5.4**). This is because the model does not consider in detail the mechanisms and modes of interaction between inlet gas jets and the rotating solids bed, which makes it impossible to generate radial and azimuthal profiles of relevant solids bed variables ($\bar{\omega}_s, \varepsilon_g, u_r$) and, thus, analyze variations of inlet gas slits. Furthermore, the angular momentum model seems to underestimate the influence on bed hydrodynamics of the inlet slit angle γ. This comes at odds with a vortex chamber predictor-response screening statistical analysis [38] that highlighted the inlet slit angle as one of the most important parameters regarding the gas pressure drop and fluidization quality of a GSVR solids bed. Still, the research mentioned was performed with Euler-Euler simulations of low-diameter vortex chambers with chimney screens to prevent particle entrainment. Hence, a more general comparative study should be undertaken to gauge the influence of each design parameter and operating condition on performance.

We could not find state-of-the-art regarding the effect of different wall materials and surface coatings on the solids bed performance in a vortex chamber. However, a method by Ortiz-Vidal et al. [39] estimates the wall drag coefficient for biphasic gas-liquid pipe flows in various flow regimes. The study proposes a modified Reynolds number that includes hydrodynamic data of each phase, including the void fraction.

In addition, Goldshtik conducted an experiment [21] that proves the validity of the quadratic drag formula for vortex chambers and estimates a drag coefficient value for multiple gas inlet velocities and the number of inlet slits on a vortex chamber. These are his conclusions:

- The quadratic drag formula is valid for the hydrodynamic modeling of vortex chambers, even though it tends to **overestimate** the magnitude of the wall resistance to the flow in most cases. This may be useful for conservative computations and first approximations to the desired hydrodynamic variables if the proposed angular momentum model is implemented, which would predict, in general, slower and less compact solids beds than experiments produce.
- The recommended monophasic wall drag coefficient is $(5 \pm 0.3) * 10^{-3}$, found by analyzing a large amount of experimental data of monophasic water flow in a vortex chamber. A value of $\mathbf{5 * 10^{-3}}$ is also suggested as a rough approximation for gas-fluid biphasic flows on the condition that the flow density takes both phases into account appropriately.

The Muschelknautz cyclone hydrodynamic model also recommends a wall-bed drag coefficient of $\mathbf{5 * 10^{-3}}$ for hydraulically smooth cyclones in a wide range of typical cyclone operating conditions [22]. Additionally, Anderson et al. estimated a wall-bed drag coefficient value of $\mathbf{3 * 10^{-3}}$ for use in their vortex chamber angular momentum model [11], based on experimental results obtained from gas-solid horizontal pipe flows in the pneumatic transport regime. One can observe that all the recommended C_f values are of the same order of magnitude, just as the fitted C_f results of previous sections. This proves the model produces consistent and accurate results even for very different design parameters and operating conditions. Moreover, Muschelknautz recommended C_f value may also elucidate the hydrodynamic and typological closeness between cyclones and vortex chamber devices, which may prove to be an essential starting point for inferences and conjectures on the behavior of vortex chamber devices while being supported by a much more mature and technically consolidated technology such as the cyclone.

Smulsky [13] suggested Prandtl's formula for the average drag coefficient of turbulent flow on a flat plate as a first approximation to the vortex chamber wall-bed drag coefficient. The formula is given in Equation 60.

$$C_f = \frac{0.077}{Re_\theta^{0.2}} \tag{60}$$

Where the azimuthal Reynolds number for the gas at the injection is defined in Equation 61.

$$Re_\theta = \frac{\rho_g (v_{in} \cos\gamma) R}{\mu_g} \quad (61)$$

The wall-bed drag coefficients predicted by this formula are shown in Table 13~~Table 13~~, along with the fitted C_f values for each dataset.

heeft opma

Table 13 Predicted wall-bed drag coefficients for all validated datasets.

Datasets			Fitted $C_f * 10^{-3}$	Smulsky $C_f * 10^{-3}$
Gonzalez-Quiroga et al.	Aluminum particles		8.53	6.47
	Walnut Shells		7.92	6.46
Kovacevic et al.	HDPE (multiple d_p)	For 1 mm	3.63	4.64
		For 1.5 mm	4.72	
		For 2 mm	5.43	
	HDPE (multiple M_s)	For 3 kg	3.25	
		For 4 kg	2.88	
		For 5.4 kg	3.27	
	Multiple ρ_s	For HDPE $\left(950 \frac{kg}{m^3}\right)$	3.85	4.32
		For Polycarbonate $\left(1240 \frac{kg}{m^3}\right)$	5.75	
Niyogi et al.	Multiple ρ_s	For 450 $\frac{kg}{m^3}$	4.58	4.88
		For 950 $\frac{kg}{m^3}$	3.78	
		For 1800 $\frac{kg}{m^3}$	4.81	
	Multiple d_p	For 0.5 mm	2.94	
		For 2 mm	5.61	

The predicted values are moderately close to the fitted values: as can be seen, both are of the same order of magnitude and have relative errors between 1.4% and 65.8%. However, Prandtl's formula proves to be insufficient to estimate the experimental C_f value on most conditions, given that it does not consider relevant parameters and operating variables that affect C_f's magnitude in complex ways and only considers the inlet gas velocity in its calculation, a variable that, as has been said, does not alter C_f's value in any significant way in the linear proportionality region of operation. Nonetheless, Prandtl's formula is the only tool to correlate the wall drag coefficient with the vortex chamber radius, which will prove instrumental for scale-up modeling.

The fitted wall-bed drag coefficients in Table 13~~Table 13~~ can be visualized in Figure 17~~Figure 17~~ to better gauge the qualitative tendencies upon the variation of each input variable.

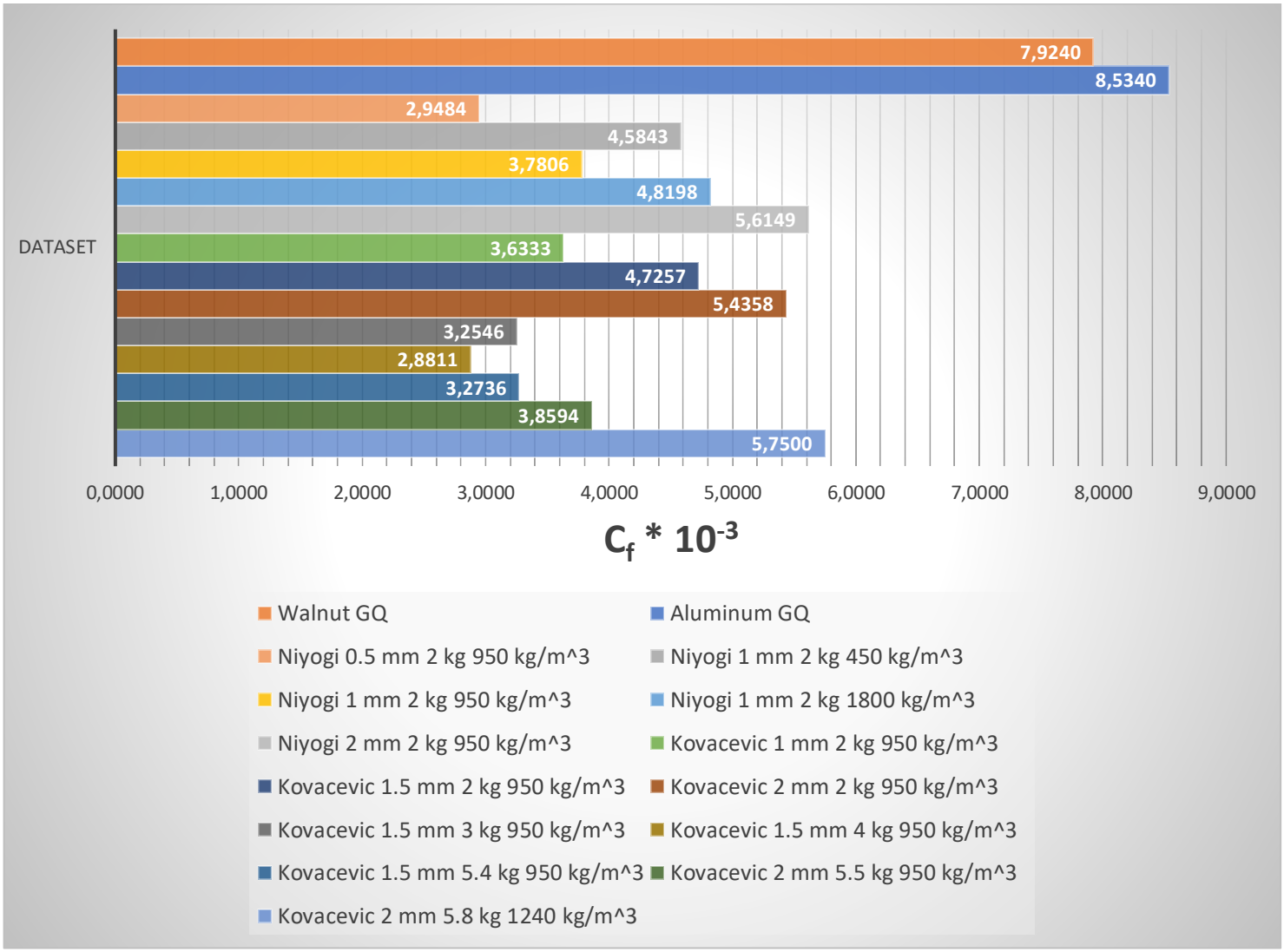

Figure 17 Bar diagram for the wall-bed drag coefficient behavior.

From Figure 17~~Figure 17~~, one can observe the following:

- C_f is strongly independent of the inlet gas velocity for 1g-Geldart B-type and D-type particles in a wide range of operating conditions.
- C_f is strongly dependent on the VC radius, taking considerably greater values, on average, for low VC radii and vice versa. This could be explained by increasing the average bed centrifugal acceleration by decreasing the chamber radius, which slows the rotating solids bed significantly through increased contact with the chamber's outer wall.

- C_f increases monotonically as the particle diameter increases. This dependency is very strong, accounting for the almost constant correlation between the average solids angular velocity and the particle diameter.
- C_f describes a positive concavity behavior concerning the solids loading, having a local minimum somewhere before the maximum solids capacity of the bed at the given conditions.
- C_f possesses a local minimum, as well, concerning particle density. This seems to depend strongly on the nearness to the bed's maximum solids capacity. Kovacevic et al. [14] found that the GSVR maximum solids capacity increases when the solids density increases and vice versa; thus, beds near or far from their maximum solids capacity produce higher C_f values than more "intermediate" beds.
- For beds analyzed at their maximum solids capacity, C_f seems to increase monotonically with particle density.

Considering the previous results, the authors conjecture that the wall drag coefficient for a gas-solid flow in a vortex chamber must depend on at least three independent factors:

- A special formulation of the azimuthal Reynolds number Re_θ^*, where the voidage fraction and additional solid phase data is included. This is in direct reference to the Cyclone body Reynolds number used for the Muschelknautz hydrodynamic model [22], where additional geometric and kinetic variables are introduced to the adimensional number; and to Ortiz-Vidal et al. [39], who devised a way to include more phenomenological information about the gas-liquid flow on the adimensional number, including the voidage fraction.
- The Swirl ratio S, as the geometrical factor that condenses the most information about the vortex intensity, general vortex chamber injection geometry, and gas residence time, according to Rosales-Trujillo et al. [20] and Gonzalez-Quiroga [1].
- A superficial parameter that describes the gas-solid flow interaction with the walls, defined here as K_{wall}. This may include the relative wall roughness k_s/R and some other granular material parameters, such as Coulomb's dynamic friction coefficient, and angle of repose, among others.

The correlation in functional form is given in Equation 62:

$$C_f = f(Re_\theta^*, S, K_{wall}) \tag{62}$$

One can also surmise further and assume an additive decomposition of C_f, by analogy to the Muschelknautz cyclone model [22], presented in Equation 63:

$$C_f = C_{f,g} + C_{f,s} \tag{63}$$

Where $C_{f,g}$ corresponds to the gas contribution to the total wall-bed drag coefficient, and $C_{f,s}$ corresponds to the solids bed contribution to the total wall-bed drag coefficient. The gas contribution to the wall-bed drag coefficient may be determined using the azimuthal

Reynolds number for the gas at the injection Re_θ, the Swirl Ratio, and the relative wall roughness k_s/R. It is presented in functional form in Equation 64:

$$C_{f,g} = f(Re_\theta, S, k_s/R) \tag{64}$$

The contribution of solids to the wall drag coefficient would be more complex. A relatively straightforward way where all of the observations in Figure 17~~Figure 17~~ may be validated is by making $C_{f,s}$ a function of the reciprocal of the total amount of particles present in the solids bed N, and the ratio of solids loading over maximum solids capacity at the operating condition M_s/M_s^{max}. By definition, in Equation 65:

$$N = \frac{M_s}{\rho_s \frac{\pi}{6} d_p^3} \tag{65}$$

A correlation for $C_{f,s}$ can be construed, given in Equation 66:

$$C_{f,s} = f\left(N^{-1}, \frac{M_s}{M_s^{max}}\right) = f\left[\left(\frac{M_s}{\rho_s \frac{\pi}{6} d_p^3}\right)^{-1}, \frac{M_s}{M_s^{max}}\right] \tag{66}$$

These tentative correlations, and others, will be explored and validated in subsequent investigations.

5.3.1 Angular momentum attenuation

One significant hydrodynamic quantity that helps describe the complicated mechanics of angular momentum transfer between gas and solid phases is the Attenuation χ. According to Kuzmin [6], it can be defined for the gas phase at the outer wall boundary in Equation 67:

$$\chi_{ow} = \frac{\Gamma_R}{\Gamma_{in}} \tag{67}$$

This quantity can be understood as a measure of the inlet gas angular momentum instantaneously transferred to the solids bed and outer wall at the periphery. This way, the less attenuation, the more the inlet gas angular momentum is dissipated at the outer wall boundary. Likewise, the quantity $1 - \chi_{ow}$ is analogous to an angular momentum transfer efficiency at the outer wall boundary. Other authors, such as Volchkov et al. [37], have treated this quantity as a normalized circulation for the gas phase. This notion extends the attenuation's definition to the entire solids bed.

Substituting **Equation (23)~~(23)~~** on **Equation (67)~~(67)~~** yields Equation 68:

$$\chi_{ow} = \frac{\sqrt{1 + \frac{2\alpha' C_{f,ow} k \bar{\rho} L_R \Gamma_{in}}{\dot{m}_g}} - 1}{\frac{\alpha' C_{f,ow} k \bar{\rho} L_R \Gamma_{in}}{\dot{m}_g}} \tag{68}$$

heeft opma
heeft opma
Cursief, Spel
heeft opma
heeft opma
heeft opma
Cursief, Spel
heeft opma

One can see similar expressions on the numerator and denominator. Letting an arbitrary variable z be on Equation 69:

$$z = \frac{\alpha' C_{f,ow} k \bar{\rho} L_R \Gamma_{in}}{\dot{m}_g} \tag{69}$$

Then, substituting **Equation (69)** in **Equation (68)** yields Equation 70:

$$\Rightarrow \chi_{ow} = \frac{\sqrt{1+2z}-1}{z} \tag{70}$$

This is the general function for gas-phase attenuation at the outer wall of a vortex chamber. **Figure 18** shows its behavior for $z \geq 0$.

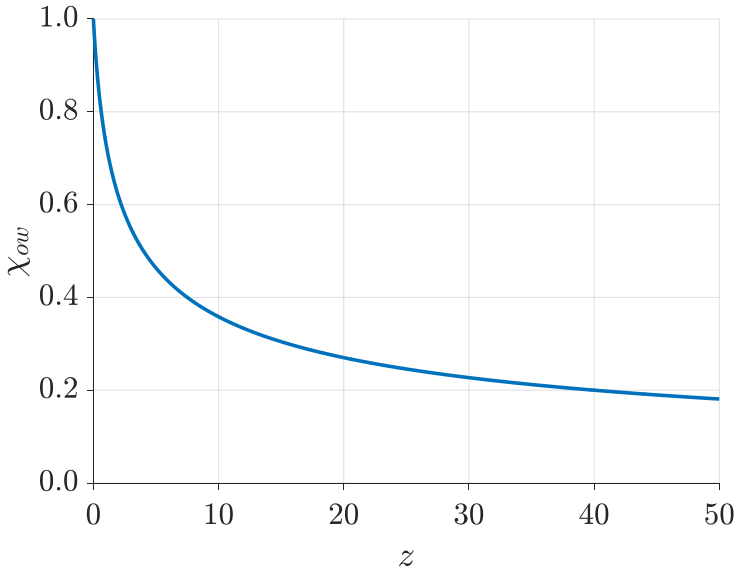

Figure 18 General behavior of the gas phase attenuation in a vortex chamber.

The outer wall attenuation seems to experience rapid changes in the interval $0 \leq z \leq 5$, after which it decays moderately slowly, finally reaching zero at infinity. The attenuation values for the datasets analyzed in this paper are found in **Table 14** for each fitted datapoint.

Table 14 Attenuation values for all analyzed datasets.

Datasets			Attenuation
Gonzalez-Quiroga et al.	Aluminum particles		0.25
	Walnut Shells		0.45
Kovacevic et al.	HDPE (multiple d_p)	For 1 mm	0.57
		For 1.5 mm	0.52
		For 2 mm	0.49

	HDPE (multiple M_s)	For 3 kg	0.58
		For 4 kg	0.61
		For 5.4 kg	0.61
	Multiple ρ_s	For HDPE $\left(950\ \frac{kg}{m^3}\right)$	0.58
		For Polycarbonate $\left(1240\ \frac{kg}{m^3}\right)$	0.51
Niyogi et al.	Multiple ρ_s	For 450 $\frac{kg}{m^3}$	0.69
		For 950 $\frac{kg}{m^3}$	0.56
		For 1800 $\frac{kg}{m^3}$	0.42
	Multiple d_p	For 0.5 mm	0.63
		For 2 mm	0.49

The general tendency here is that denser and bigger particles in a highly loaded solids bed rotating in a small vortex chamber have a lower outer wall attenuation than other rotating beds. Of course, this does not imply that the resulting beds are necessarily faster and more compact but that the angular momentum transfer efficiency is the greatest for these kinds of beds, which is aligned with previous research for CFBs and centrifugal fluidized beds [12][24][25][40].

5.4 Outlook

The previous sections discussed an angular momentum balance model for the GSVR. As it stands, the model's formulation only involved key measurable hydrodynamic quantities for the solids bed, like the average solids bed angular velocity $\bar{\omega}$, the average void fraction ε_g, and the average inner bed edge radius r_b. However, the proposed model is capable of quantifying and gauging the sensitivity of other output variables of interest, like the following:

- Average solids azimuthal velocity
- Average solids centrifugal acceleration
- Average gas-solid azimuthal slip velocity
- Average solids fraction
- Radial profile of the gas azimuthal velocity

The model may also help to solve design-type problems regarding what value a certain geometric parameter or particle property should take to produce a determined solids bed. This inverse procedure is fundamental for vortex chamber PI potential and scalability, given the considerable computational hurdles involved in CFD parametric studies, even for 2D analyses [25] [38]. Thus, there is a great incentive to study other vortex chamber typologies and explore improvement opportunities to conventional vortex chamber design with the proposed model, taking advantage of its simplicity and robustness.

For example, one can consider a monolayer of coarse particles rotating alongside the solids bed at the outer wall, acting as a buffer between both in such a way that minimizes the outer wall resistance $\mathcal{R}_{ow}$ of the solids bed, increasing the bed's azimuthal velocity and acceleration [1], [12]. One can also consider secondary gas injection at an end wall, first proposed by Anderson et al. as early as 1972 [11], which vastly increases the inlet angular momentum available to the solids bed and reduces the end wall resistance $\mathcal{R}_{ew}$ and particle entrainment through the chimney. Another way to improve vortex chamber performance may lie in modifying inlet slit geometry such that a change in inlet slit area and shape (and a consequent change in inlet angular momentum) is accompanied by a great decrease in end wall resistance $\mathcal{R}_{ew}$ and increase in solids bed uniformity. Additionally, a change in the outer wall geometry from a circular to a polygonal shape may induce a beneficial Coandă effect near the gas flow at the outer wall, one that can, in principle, push out particles approaching the outer wall and, thus, reduce the outer wall resistance $\mathcal{R}_{ow}$ by decreasing particle-wall friction and collisions. One can even consider rotating end walls with the proposed model, such as the novel STARVOC reactor [41] that combines the advantages of both RFB and vortex chamber technologies into a single compact and efficient contactor. Lastly, ultrasound and magnetic levitation techniques (for paramagnetic particle beds) can be analyzed and implemented on the VC walls to counteract bed nonuniformities; improve mixing, heat, and mass transfer; and reduce wall-particle contact times, analogous to the action of Vibrating Fluidized Beds (VFB) [42]; and consequently, producing faster and more uniform rotating beds.

The proposed model can also help in scale-up procedures, as the inclusion of relevant VC geometric parameters, such as chamber diameter, chamber length, and slit number, enable scaling chamber dimensions and solids loadings while maintaining the same overall bed behavior and vortex chamber performance. This is a significant corollary, given that no other quantitative scale-up method has been found in vortex chamber literature. At the same time, common approaches solely constrain themselves to CFD and experiments at lab-scale operation. Considering the significant cost, computational time and power, and validation procedures needed to verify similarity and predict vortex chamber scale-up outcomes, this technology has still not seen commercial deployment. Predictability and controllability of a centrifugal contactor are a priority as with any other industrial equipment. For instance, the proposed model is capable of determining the chamber diameter D necessary to produce a desired average solids angular velocity $\bar{\omega}_s$ by selecting specific parameters like the desired centrifugal field intensity G, inlet gas velocity v_{in}, aspect ratio $\frac{L_R}{R}$, solids loading M_s, and slit number I_N, as well as providing graphs detailing correlations between these parameters around a single point of operation.

While the previous prospects look promising, improvements must be made to the model. A consensus needs to be reached facing a standard definition of the vortex chamber average inner bed edge radius and fluidization criteria, which are necessary to compute the average solids azimuthal velocity and acts as a reference frame to compare different C_f values for widely different bed conditions and chamber sizes. Niyogi et al. [19] proposed a criterion

defining the location of the inner bed edge radius where the static pressure reached a sustained minimum value. They used it to calculate average azimuthal velocities despite having direct measurements of the average inner bed edge radius. This could be a promising and easy-to-implement criterion, given the difficulties regarding the location of an actual inner bed edge radius for dilute or unstable beds. Additionally, the results and conjectures regarding the gas injection expansion factor k and wall-bed drag coefficient C_f need to be validated with a greater and broader selection of input data while also considering a continuous mode of operation for the vortex chamber. Moreover, improving the model to consider different inlet slit geometries and sinusoidal solids bed velocity profiles may be the key to optimizing the performance and design of the vortex chamber, albeit with an inevitable increase in complexity and computational cost.

6 CONCLUSION

An angular momentum model was formulated for the GSVR following the works of various authors. Literature reports many attempts to develop a simple yet reliable analytical approach to vortex chamber cold hydrodynamics, but none could provide a systematic and tractable 2D method that considered the whole solids bed and accounted for key quantities like solids azimuthal velocity, inner bed edge radius, and void fraction. The proposed model is based on angular momentum balances over the solids bed, from the gas inlet slits to the inner bed edge region, while considering the gas flow and solids bed motion as a biphasic flow. Elaborating upon results from previous authors, important hydrodynamic parameters were introduced, such as wall-bed drag coefficients for the outer wall and end walls $C_{f,ow}, C_{f,ew}$, and the gas injection expansion factor k, along with some insights into their inferred correlations to relevant flow variables and operation parameters. Furthermore, a method to close the proposed non-linear algebraic equations was developed based on well-known gas-solid drag equations, highlighting the applicability of Ergun's model and Gibilaro's model in a simplified radial force balance on the solids bed. Finally, the model culminated in the novel definition of angular momentum resistances that describe the influence of the three most essential solids bed boundaries: the gas inlets, the outer wall, and the end walls, with their respective analogs for gas-only GVU flows.

The model was validated with three independent sets of batch operation GSVR data for 1g-Geldart B-type and D-type particles, out of which two datasets were experiment-based, and one was CFD-based. Caution was had regarding how flow variables were measured for each dataset and input into the model, most notably, the inner bed edge radius for each condition. Parity plots and average solids azimuthal velocity vs. gas injection velocity plots were presented for relevant subsets of each dataset, with particular attention to the merged wall-bed drag coefficient's sensitivity to changes in gas injection velocity, solids loading, particle diameter, particle density, and chamber radius. The results were significant enough to ascertain the independence of C_f to the gas injection velocity in the studied operational range, more data is needed to gauge its dependence on other operational parameters. Still, qualitative

monotonic dependencies could be constructed for most of them, all of which agree with known research on vortex chamber hydrodynamics.

In conclusion, the proposed model predicted a vast quantity of one-on-one/*ceteris paribus* correlations between operational parameters and three key flow variables, relationships that make physical and mathematical sense and strongly match experimental and CFD-based vortex chamber literature. This concise and comprehensive quality of the model, along with its capability to predict end wall braking effects being one order of magnitude greater than outer wall and gas injection braking effects, make the angular momentum model a useful tool to predict vortex chamber performance, analyze and compare different vortex chamber typologies and improvement opportunities to vortex chamber operation, and potentially aid in future scale-up endeavors with minimal uncertainty and computational complexity.

7 REFERENCES

[1] A. Gonzalez-Quiroga *et al.*, "Azimuthal and radial flow patterns of 1g-Geldart B-type particles in a gas-solid vortex reactor," *Powder Technology*, vol. 354, pp. 410–422, 2019, doi: 10.1016/j.powtec.2019.06.015.

[2] B. S. Sazhin, L. M. Kochetov, and A. S. Belousov, "Retention capacities and flow patterns of vortex contactors," *Theoretical Foundations of Chemical Engineering*, vol. 42, no. 2, pp. 125–135, 2008, doi: 10.1134/S0040579508020036.

[3] M. Friedle, K. Niyogi, M. M. Torregrosa, G. B. Marin, and G. J. Heynderickx, "A drag model for the gas-solid vortex unit," *Powder Technology*, vol. 312, pp. 210–221, 2017, doi: 10.1016/j.powtec.2017.02.012.

[4] M. Friedle, G. B. Marin, and G. J. Heynderickx, "Operational range of a Gas-Solid Vortex Unit," *Powder Technology*, vol. 338, pp. 702–715, 2018, doi: 10.1016/j.powtec.2018.07.062.

[5] A. de Broqueville and J. de Wilde, "Numerical investigation of gas-solid heat transfer in rotating fluidized beds in a static geometry," *Chemical Engineering Science*, vol. 64, no. 6, pp. 1232–1248, 2009, doi: 10.1016/j.ces.2008.11.009.

[6] A. O. Kuzmin, "Confined multiphase swirled flows in chemical engineering," *Reviews in Chemical Engineering*, 2020, doi: 10.1515/revce-2019-0019.

[7] M. L. Rosenzweig, W. S. Lewellen, and D. H. Ross, "Confined vortex flows with boundary-layer interaction," *AIAA Journal*, vol. 2, no. 12, pp. 2127–2134, 1964, doi: 10.2514/3.2753.

[8] D. N. Wormley, "An analytical model for the incompressible flow in short vortex chambers," *Journal of Fluids Engineering, Transactions of the ASME*, vol. 91, no. 2, pp. 264–272, 1969, doi: 10.1115/1.3571091.

[9] E. P. Volchkov, S. V. Semenov, and V. I. Terekhov, "Aerodynamics of end-wall boundary layer in a vortex chamber," *Journal of Applied Mechanics and Technical Physics*, vol. 27, no. 5, pp. 740–748, 1986, doi: 10.1007/BF00916149.

[10] M. A. Gol'dshtik and S. S. Dashin, "Hydraulic resistance of swirl chambers with a fluid layer," *Journal of Applied Mechanics and Technical Physics*, vol. 33, no. 1, pp. 48–52, 1992, doi: 10.1007/BF00864503.

[11] L. A. Anderson, S. H. Hasinger, and B. N. Turman, "Two-component vortex flow studies of the colloid core nuclear rocket," *Journal of Spacecraft and Rockets*, vol. 9, no. 5, pp. 311–317, 1972, doi: 10.2514/3.61678.

[12] L. A. Vandewalle, A. Gonzalez-Quiroga, P. Perreault, K. M. van Geem, and G. B. Marin, "Process intensification in a gas-solid vortex unit: Computational fluid

dynamics model based analysis and design," *Industrial and Engineering Chemistry Research*, vol. 58, no. 28, pp. 12751–12765, 2019, doi: 10.1021/acs.iecr.9b01566.

[13] J. J. Smulsky, "The mathematical models of the rotated layers," in *Third International Conference on Multiphase Flow*, 1998, p. 6.

[14] J. Z. Kovacevic, M. N. Pantzali, G. J. Heynderickx, and G. B. Marin, "Bed stability and maximum solids capacity in a Gas-Solid Vortex Reactor: Experimental study," *Chemical Engineering Science*, vol. 106, pp. 293–303, 2014, doi: 10.1016/j.ces.2013.11.018.

[15] J. De Wilde and A. de Broqueville, "Rotating fluidized beds in a static geometry: Experimental proof of concept," *AIChE Journal*, vol. 53, no. 4, pp. 793–810, Apr. 2007, doi: 10.1002/aic.11139.

[16] B. N. Turman and S. H. Hasinger, "Experimental flow studies of the colloid core reactor concept," *Journal of Spacecraft and Rockets*, vol. 9, no. 10, pp. 723–724, 1972, doi: 10.2514/3.61791.

[17] B. Sreenivasan and V. R. Raghavan, "Hydrodynamics of a swirling fluidised bed," *Chemical Engineering and Processing*, vol. 41, no. 2, pp. 99–106, 2002, doi: 10.1016/S0255-2701(00)00155-0.

[18] J. Z. Kovacevic, M. N. Pantzali, K. Niyogi, N. G. Deen, G. J. Heynderickx, and G. B. Marin, "Solids velocity fields in a cold-flow gas-solid vortex reactor," *Chemical Engineering Science*, vol. 123, pp. 220–230, 2015, doi: 10.1016/j.ces.2014.10.020.

[19] K. Niyogi, M. M. Torregrosa, M. N. Pantzali, G. J. Heynderickx, and G. B. Marin, "Experimentally validated numerical study of gas-solid vortex unit hydrodynamics," *Powder Technology*, vol. 305, no. x, pp. 794–808, 2017, doi: 10.1016/j.powtec.2016.10.049.

[20] W. R. Trujillo and J. De Wilde, "Influence of solids outlets and the gas inlet design on the generation of a gas-solids rotating fluidized bed in a vortex chamber for different types of particles," *Chemical Engineering Science*, vol. 173, pp. 74–90, 2017, doi: 10.1016/j.ces.2017.07.031.

[21] M. A. Gol'dshtik and N. I. Sobakinskikh, "Friction of fluid flow against the end-face surfaces of vortex chambers," *Journal of Applied Mechanics and Technical Physics*, vol. 23, no. 3, pp. 353–354, 1982, doi: 10.1007/BF00910072.

[22] A. C. Hoffmann and L. E. Stein, *Gas cyclones and swirl tubes: Principles, design and operation*, 2nd ed. Springer-Verlag Berlin Heidelberg, 2008. doi: 10.1007/978-3-540-74696-6.

[23] R. P. Dring and M. Suo, "Particle Trajectories in Swirling Flows.," *J Energy*, vol. 2, no. 4, pp. 232–237, 1978.

[24] M. Filla, L. Massimilla, and S. Vaccaro, “Gas jets in fluidized beds: The influence of particle size, shape and density on gas and solids entrainment,” *International Journal of Multiphase Flow*, vol. 9, no. 3, pp. 259–267, 1983, doi: 10.1016/0301-9322(83)90105-2.

[25] A. Dutta, R. P. Ekatpure, G. J. Heynderickx, A. de Broqueville, and G. B. Marin, “Rotating fluidized bed with a static geometry: Guidelines for design and operating conditions,” *Chemical Engineering Science*, vol. 65, no. 5, pp. 1678–1693, 2010, doi: 10.1016/j.ces.2009.11.013.

[26] S. R. Kulkarni *et al.*, “An experimental and numerical study of the suppression of jets, counterflow, and backflow in vortex units,” *AIChE Journal*, vol. 65, no. 8, pp. 1–13, 2019, doi: 10.1002/aic.16614.

[27] B. S. Sazhin, L. M. Kochetov, and A. S. Belousov, “Retention capacities and flow patterns of vortex contactors,” *Theoretical Foundations of Chemical Engineering*, vol. 42, no. 2, pp. 125–135, 2008, doi: 10.1134/S0040579508020036.

[28] K. Niyogi, M. M. Torregrosa, M. N. Pantzali, G. J. Heynderickx, G. B. Marin, and V. N. Shtern, “On Near-Wall Jets in a Disc-Like Gas Vortex Unit,” vol. 63, no. 5, 2017, doi: 10.1002/aic.

[29] E. Keshock and J. Savino, “Experimental profiles of velocity components and radial pressure distributions in a vortex contained in a short cylindrical chamber,” Cleveland, Ohio, 1965.

[30] L. T. Fan and C. C. Chang, “Incipient Fluidization Condition for a Centrifugal Fluidized Bed,” vol. 31, no. 6, pp. 999–1009, 1985.

[31] Y. -M Chen, “Fundamentals of a centrifugal fluidized bed,” *AIChE Journal*, vol. 33, no. 5, pp. 722–728, 1987, doi: 10.1002/aic.690330504.

[32] S. Ergun, “Fluid Flow through packed columns,” *Chemical engineering progress*. pp. 89–94, 1952.

[33] L. G. Gibilaro, *Fluidization Dynamics*, 1st Editio. Butterworth-Heinemann, 2001.

[34] S. Shamkuwar, D. Malkhede, N. Chopra, P. Dange, N. Chandratre, and R. Damle, “A novel approach of centrifugal fluidized chamber to remove diesel engine particulate matter emission,” *International Journal of Ambient Energy*, vol. 0, no. 0, pp. 1–9, 2019, doi: 10.1080/01430750.2019.1636879.

[35] M. N. Pantzali, J. Z. Kovacevic, G. J. Heynderickx, and G. B. Marin, “Guidelines for selecting GSVR operating conditions based on hydrodynamic characteristics.pdf,” Ghent, Belgium.

[36] S. Dutta, C. Loha, P. K. Chatterjee, A. Kumar Sadhukhan, and P. Gupta, “Numerical investigation of gas-particle hydrodynamics in a vortex chamber fluidized bed,”

Advanced Powder Technology, vol. 29, no. 12, pp. 3357–3367, 2018, doi: 10.1016/j.apt.2018.09.014.

[37] E. P. Volchkov, N. A. Dvornikov, V. V Lukashov, and R. K. Abdrakhmanov, "Investigation of the flow in the vortex chamber with centrifugal fluidizing bed with and without combustion," vol. 20, no. 6, pp. 663–668, 2013.

[38] Z. Lavrich, D. R. Wagner, Z. Taie, D. Halliday, and C. L. Hagen, "Design considerations for small scale rotating fluidized beds in static geometry with screens for fine particles," *Chemical Engineering Research and Design*, vol. 137, pp. 89–100, 2018, doi: 10.1016/j.cherd.2018.06.044.

[39] L. E. Ortiz-vidal, N. Mureithi, and O. M. H. Rodriguez, "Friction Factor in Two-Phase Gas-Liquid Pipe Flow Friction Factor in Two-Phase Gas-Liquid Pipe Flow," no. January, 2013.

[40] M. Pore *et al.*, "Particuology Magnetic resonance studies of a gas – solids fluidised bed : Jet – jet and jet – wall interactions," vol. 8, pp. 617–622, 2010, doi: 10.1016/j.partic.2010.07.015.

[41] A. Gonzalez-Quiroga, V. Shtern, P. Perreault, L. Vandewalle, G. B. Marin, and K. M. van Geem, "Intensifying Mass and Heat Transfer using a High-g Stator-Rotor Vortex Chamber," *Chemical Engineering and Processing - Process Intensification*, vol. 169, Dec. 2021, doi: 10.1016/j.cep.2021.108638.

[42] H. Jin, Z. Tong, J. Zhang, and B. Zhang, "Homogeneous Fluidization Characteristics of Vibrating Fluidized Beds," *The Canadian Journal of Chemical Engineering*, vol. 82, no. 5, pp. 1048–1053, 2008, doi: 10.1002/cjce.5450820521.